Contrast-Enhanced Optical Coherence Tomography Using Gold Nanorods

By

Andrew Young Gordon

Dissertation

Submitted to the Faculty of the

Graduate School of Vanderbilt University

in partial fulfillment of the requirements

for the degree of

DOCTOR OF PHILOSOPHY

in

Molecular Physiology and Biophysics

June 30, 2019

Nashville, Tennessee

Approved:

David Wasserman, Ph.D.

John Penn, Ph.D.

Craig Duvall, Ph. D.

Rachel Kuchtey, M.D., Ph.D.

To my family, with love, thank you for your support

Acknowledgments

I received a lot of support in many forms and from a number of sources while I was doing the work presented here. I would like to thank Ash Jayagopal, for helping rekindle my interest in scientific research while I was in medical school, and for being an excellent advisor during my first years of graduate school.

I would like to particularly thank John Penn. I first met John eight or so years ago as a medical student. I never imagined I would end up working in his lab, but he was kind enough to accept me as a graduate student when I needed somewhere to finish my research after Ash left. More than that, he was wise and patient enough to shepherd both me and my research to a satisfactory conclusion. I will always be grateful for his help and guidance over the years.

I would like to thank my other dissertation committee members, Dr. Wasserman, my committee chair, Dr. Kuchtey, and Dr. Duvall, for being reliable sources of good advice that improved my work as I pursued my research goals. Dr. Wasserman was also kind enough to take over as chair when John became my advisor, which I appreciate.

I have had the chance to work with some outstanding scientists, graduate students, and research assistants in multiple labs during my time in graduate school. There are too many people to list here, but please know that I am a better scientist for having worked with all of you.

During most of my time in graduate school, I was a trainee under the auspices of the Vanderbilt Vision Research Center. This work would not have been possible without the support of both the VVRC and the Vanderbilt Eye Institute.

Last, but certainly not least, I would like to thank my family. My time in graduate school has been rewarding, but not without its difficulties. I knew I always had my family behind me, and that has made all of the difference. Thank you.

Table of Contents

Page

List of Tables

Page

Table

List of Figures

Page

Figure

Chapter 1: Introduction to Gold Nanorods and Their Application to Optical Coherence Tomography

Introduction

In the field of ophthalmology, optical coherence tomography (OCT) is an imaging modality that is widely used in the clinical setting while also being a valuable tool for researchers[1]. OCT non-invasively provides fast, high-resolution information about the structure of the tissues it images. Clinically, this allows it to detect changes caused by age-related macular degeneration (AMD), diabetic retinopathy (DR), and glaucoma[2–4]. These diseases are among the most common causes of irreversible vision loss in the developed and developing world.

Despite the obvious clinical utility of OCT, it can currently only detect a disease when it has progressed to the point of causing structural change to the tissue being imaged. This shortcoming is most acute in the retina because many diseases affecting that tissue can cause vision loss prior to, or concurrent with, changes in tissue structure that are visible on standard OCT[5,6]. The research presented in this dissertation will address this significant limitation by increasing the amount of information that can be generated by OCT systems when performing retinal imaging. More specifically, we want to move beyond simple structural assessments of retinal morphology into functional assessments of physiology or molecular expression.

To achieve this goal we seek to enhance the native strengths of OCT systems by introducing contrast agents that respond to physiological or molecular changes in tissue by altering their concentration therein. If an OCT system can detect these changes in contrast agent concentration, it will gain the ability to report on physiological and structural changes in tissue simultaneously while maintaining its high spatial resolution. Creating contrast agents that are compatible with OCT systems is difficult because the systems use a coherent light source to

create images of tissue, and any contrast agent that destroys this coherence, such as a fluorophore, is largely invisible to OCT systems natively.

So, to generate contrast using OCT systems, a contrast agent needs to absorb or reflect light in the spectral range emitted and detected by the system, while being able to reach the tissue being imaged[7]. We use gold nanorods (GNR) for this purpose. GNR are excellent candidates for OCT contrast-enhancement because their absorption and reflectivity are tunable in degree and wavelength, and they are amenable to versatile surface functionalization[8]. Additionally, since gold itself is generally considered biocompatible GNR are a viable candidate for clinical translation. In this dissertation we will present a number of studies involving the functionalization and delivery of GNR, as well as the retinal imaging of GNR using standard OCT systems.

The retina presents a particularly difficult target for contrast-enhancement of OCT because it has a wide range of reflectivity in its different layers. This becomes a more significant issue in disease states, or animal models of disease states, that further create heterogeneous tissue reflectivity. This variable reflectivity is naturally at odds with the detection of a contrast agent that changes reflectivity and makes it difficult to detect GNR using standard OCT technology.

We address this issue by combining OCT adjuncts and GNR technology. OCT adjuncts work in conjunction with OCT systems to enhance them in some way, usually by providing them with more information to assess or by altering how existing data is processed. These improvements can allow for the detection of contrast agents where previously it was impossible. Along those lines, we will also present a number of studies related to the imaging of GNR *in vivo* and *in vitro* using OCT adjunct imaging systems.

Background

The studies we present are at the intersection of retinal physiology, optical coherence tomography, and gold nanorod biochemistry. For the remainder of this chapter, we will present background information that helps in understanding these technologies, with an emphasis on those that are relevant to our studies.

Optical Coherence Tomography

Optical coherence tomography is a non-invasive imaging modality developed in the early 90s that offers micron-scale resolution images tissue structure at a speed that is unmatched by any other imaging modality[1]. Its principal drawback is its relatively poor depth of penetration. Given these characteristics, OCT has become a clinical gold standard for ocular imaging, since that organ allows for excellent light penetration. It is also a versatile research tool, with a number of emerging applications being studied including cancer imaging, lymph node imaging, and imaging of blood flow and immune response[9].

In terms of function, optical coherence tomography has been called "ultrasound with light" because it measures the degree to which light in the UV-vis spectrum bounces off of its target. While this is a fitting analogy, the reality of how OCT operates is considerably more complex, and some understanding is necessary to appreciate the challenge and opportunities associated with enhancing optical coherence tomography imaging using adjunct technologies or exogenous contrast agents.

It is impossible using existing technologies to detect the distinct returning pulses of light emitted by retinal tissues that are spaced tens of microns apart. Given the speed of light, the returning signals would be separated in time by femtoseconds. As a result, OCT systems actually

detect standing interference patterns created by a light source interacting with itself, after being split into a beam going to the sample arm or a reference arm. This interference pattern allows OCT systems to determine the degree and depth of reflectivity in the imaging target. As a result, the basic measurement reported by optical coherence tomography systems is reflectivity versus depth[1]. It is important that the light source is minimally coherent as this determines the resolution of the resulting images. The coherence length of an OCT beam dictates over what physical distance the light is capable of interfering with itself. A shorter coherence length is the product of a broader spectrum (less coherent) light source[10]. The broader the spectrum of the light source, the shorter the coherence length, and the better the axial resolution of the resulting measurement[1]. This single measurement is known as an A-scan. By iterating this process across a tissue, multiple A-scans can be collated into a B-scan, and ultimately a three-dimensional representation of the imaged tissue can be formed by combining multiple B-scans. Recent advances in native optical coherence tomography imaging systems have focused on improving its already impressive spatial resolution in addition to other enhancements in overall image quality[11,12].

Retinal Anatomy on OCT

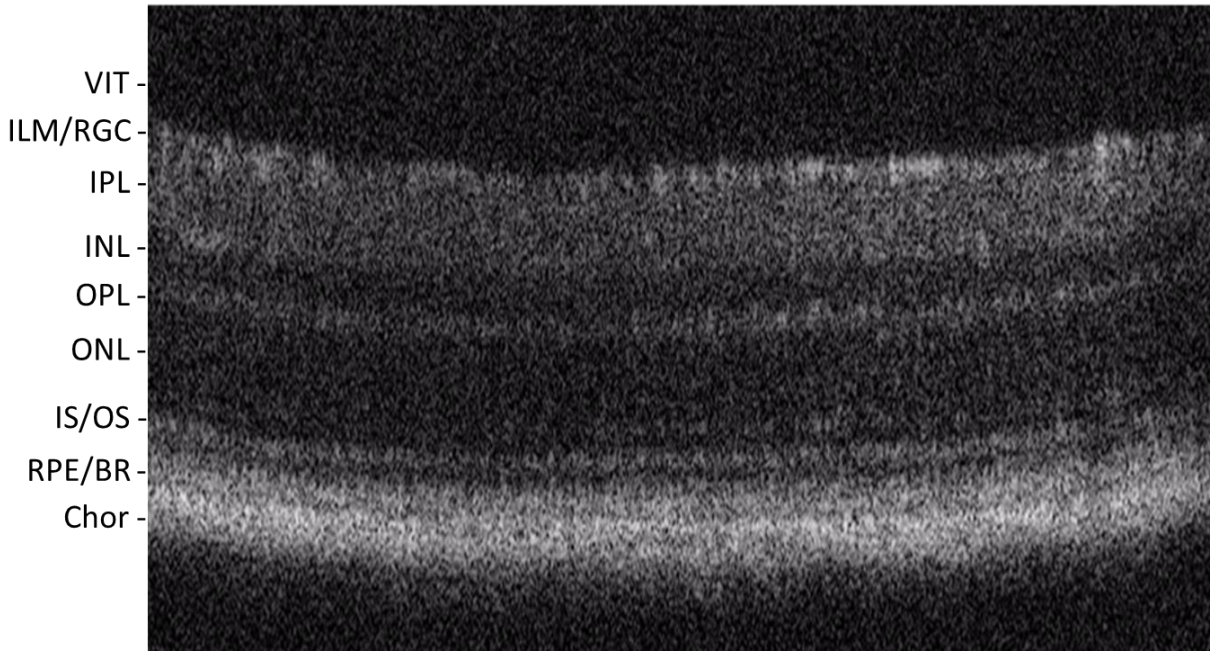

Figure 1: The Mouse Retina on OCT. Note that like all standard OCT images, the data is presented in grayscale. Legend: vitreous humor (VIT), inner limiting membrane (ILM), retinal ganglion cell layer (RGC), inner and outer plexiform and nuclear layers (IPL, INL, OPL, ONL), photoreceptor inner and outer segments (IS/OS), retinal pigemented epithelium (RPE), Bruch's membrane (BR), and the choroid (Chor).

As the studies presented here are largely concerned with retinal imaging using OCT, a brief aside regarding retinal anatomy as it appears on OCT is prudent. Figure 1 is example of the quality of retinal imaging available using a standard, commercial OCT system for rodent eyes. Light would be approaching this retina from the top of the screen, and the uppermost part of the retina on this image is the inner retina. The innermost retina is comprised of the inner limiting membrane (ILM) which is a barrier to movement from the vitreous into the retina. The retinal ganglion cell (RGC) layer, axons from which become the retinal nerve fiber layer that merges to become the optic nerve at the optic nerve head, is directly adjacent. Moving further back into the retina (down on the image) are the inner plexiform and nuclear layers (IPL, INL) and outer plexiform and outer nuclear layers (OPL, ONL). These layers are comprised of neurons that

communicate between RGCs and the outer layers of the retina, which contain rod and cone photoreceptors. The rods and cones are the base functional units of vision, responding to photons by undergoing rapid physiological and ultimately electrochemical changes that are communicated to the visual processing centers of the brain via the neuroretinal pathways just discussed. They have inner and outer segments (IS/OS) which are not clearly distinguished in Figure 1. Just behind the rods and cones is the retinal pigmented epithelium (RPE), which is very bright on OCT. Bruch's membrane (BR), which is on the border of the retina and the choroid (Chor), is also present in that area. The choroid is an important blood supply to the outer retina. These layers of the outer retina and inner choroid are sometimes difficult to distinguish from one another, as is demonstrated by Figure 1.

Contrast Agents in Optical Coherence Tomography

While optical coherence tomography is a light-based imaging modality, the design of contrast agents that are compatible with it is complicated by the requirement that the minimal coherence of the light source be maintained during and after its interaction with the contrast agent. For this reason, fluorophores and other dyes standardly used to provide contrast with light-based imaging modalities are not generally detected by optical coherence tomography systems[13].

There are a number of contrast agents that have been studied for use with optical coherence tomography and its adjuncts, primarily because of their ability to interact with the wavelengths of light emitted and detected by optical coherence tomography systems, or interact in some way with the adjunct systems. Notable examples of potential exogenous contrast agents include ferrous nanoparticles[14], light-absorbing dyes (e.g. indocyanine green)[15], polystyrene beads, or gold nanoparticles[16]. Of these, we think the most promising for contrast enhancement

of OCT is the gold nanoparticle, in particular GNR because its unique optical properties allow it to interact very strongly with the light emitted and detected by OCT systems.

The Synthesis of GNR and Their Optical Properties

The most common and facile method of GNR synthesis is called wet synthesis, and it involves seeding a mixture of colloidal gold and cetyltrimethylammonium bromide in order to begin the process of GNR growth[17]. By altering relative concentrations of reactants and reaction times a variety of GNR can be made with variable lengths and widths[18]. This length-to-width (or "aspect") ratio of the GNR governs the wavelength with which it maximally interacts[8]. This wavelength is known as its surface plasmon resonance (SPR), which is an effect caused by collective oscillations of electrons on the GNR surface. At this SPR wavelength, the GNR both absorbs and reflects light strongly relative to its size, which is a valuable property for an OCT contrast agent. The degree to which the light is absorbed versus reflected is related to the overall size of the nanorod. The nature of a GNR's interaction with light has had considerable experimental verification[19]. This means that the optical properties of GNR are quite tailorable depending on their desired application. Figure 2 depicts a standard GNR as seen using transmission electron microscopy (TEM).

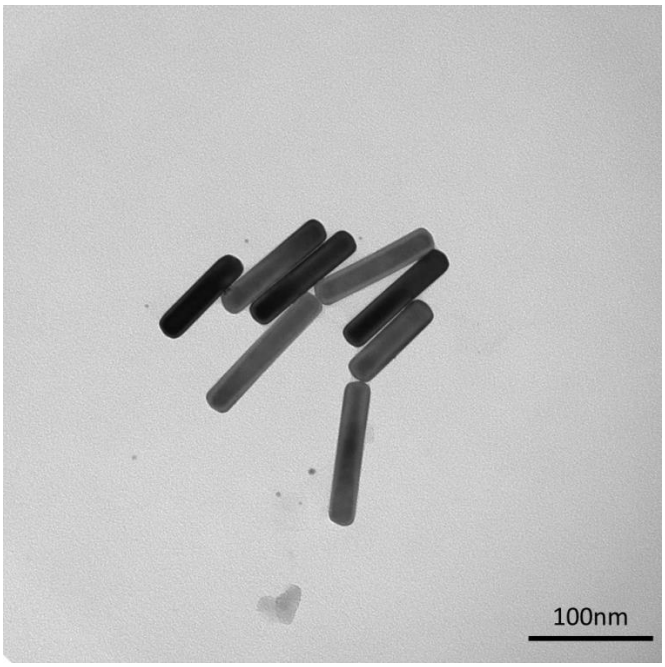

Figure 2: Representative TEM image of GNR. This figure shows bare GNR with a typical shape.

Gold Nanorod Detoxification, Delivery, and Targeting

With these optical properties, GNR are an ideal contrast agent for OCT imaging modalities. The problem then becomes one of stabilization and delivery of the nanoparticles to a place where they can be successfully imaged. Wet synthesis of gold nanorods leaves a CTAB coating on the particle. The stability of the GNR in solution is dependent on its CTAB concentration. Unfortunately the necessary concentration of CTAB is cytotoxic, immunogenic, and potentially disruptive to OCT imaging applications[20].

This means that there is the need for a coating that prevents nanoparticle aggregation and is not cytotoxic. A number of coatings have been studied with suitable properties, and they can be broadly grouped into two categories[21]. First, electrostatic coatings rely on creating and maintaining a surface charge on the gold nanoparticle that is of sufficient strength to repulse similarly charged nearby nanoparticles[22]. While CTAB itself would technically fall into this category, these coatings can be applied and maintained in such a way that they are not reliant on

solute concentration for their stability in solution, or following injection. The major drawback of this class of coatings is that while their charge is self-repulsive, it can attract oppositely charged molecules *in vivo*.

The second class of stabilizing coatings is the steric inhibitors, which broadly rely on their bulk rather than charge to prevent aggregation of nanoparticles[23]. As these are usually covalently bonded to the gold surface, they retain their aggregation-preventing properties both in solution and following injection[24]. While their lack of surface charge can reduce the interaction of these nanoparticles with other biological components, their large size can potentially make delivery more difficult[25]. Polyethylene glycol, which features heavily in the GNR constructs used in our studies, is a member of this group[26].

Optical Coherence Tomography Adjuncts

As previously mentioned, optical coherence tomography systems natively only provide reflectivity versus depth information, which can be a limitation in heterogeneous tissue. In an effort to address this deficiency and provide more informative OCT images, researchers have combined novel imaging technologies with OCT systems in what are known as OCT adjuncts[27].

One OCT adjunct system is photothermal OCT (PT-OCT)[28]. This technology uses an additional laser source to heat the tissue being imaged in a pulsed fashion. This heating alters the temperature of the surrounding media. This temperature change alters the refractive index of the surrounding media, which changes the optical path length of the light detected by OCT systems through that media. By detecting these periodic changes in optical path length it is possible to determine the degree to which a given tissue absorbs the light emitted by the photothermal light source. This technology offers another dimension along which to distinguish between tissue

types or exogenous contrast agents. PT-OCT is compatible with GNR contrast agents because GNR can absorb light and emit it as heat, thereby generating a photothermal (PT) signal[16,29].

Another OCT adjunct is spectroscopic OCT, which includes split-spectrum and spectral-fractionation optical coherence tomography (SF-OCT). These technologies probe the entire spectrum of light emitted and detected by an optical coherence tomography system in order to measure changes in tissue reflectivity across narrower bands of this spectrum[30]. This allows for the generation of data relating to the spectrum of light reflected by tissue or a contrast agent. A significant drawback of this technology is that there is an inherent trade-off between spectral and spatial resolution in the system. However, with native optical coherence tomography systems approaching sub-micron axial resolutions, this trade-off could be favorable under a number of circumstances. SF-OCT is compatible with GNR contrast agents because the spectrum across which GNR maximally reflects light can be offset relative to the SF-OCT system's emission spectrum, creating the spectral contrast the system is designed to detect[30].

There are several additional adjunct optical coherence tomography systems used in research settings. Photoacoustic optical coherence tomography relies on the photoacoustic effect, the emission of sound waves by certain particles after they have absorbed energy at a certain wavelength, to pinpoint the location of relevant particles in the tissue being imaged[31,32]. Like photothermal optical coherence tomography, this approach requires an additional laser source to be integrated into the imaging system. Unlike photothermal optical coherence tomography, it also requires an additional detector to pinpoint the emitting sound waves in the tissue[33]. Pump-probe OCT detects dyes by acquiring an optical coherence tomography image, photobleaching the dyes with a second integrated light source, and reacquiring the image to detect changes due to the bleaching[15]. Magnetomotive OCT uses the manipulation of ferromagnetic particles by

external magnetic fields to alter the tissue in a way that can be detected by OCT systems, although this requires some way to administer that field concurrent with the imaging, as well as ferromagnetic contrast agents[14,34].

Chapter 2: Gold Nanorod Detoxification, Functionalization, and OCT Imaging

Introduction

Despite the desirability of gold nanorods as optical coherence tomography contrast agents, there are significant barriers to their effective use in *in vivo* ocular imaging. To be a viable candidate, the GNR construct must be stable both in solution and after injection. Instability in this case refers to the aggregation of GNR that occurs readily if the surface coating does not sterically or electrostatically inhibit it. This aggregation alters the optical properties of the GNR, thus compromising their utility as contrast agents[35].

An early study using OCT to image intravitreally injected GNR showed the formation of opacities of unknown composition following intravitreal injection of bare GNR in conjunction with an immune response to the injections[36]. It was unclear what caused this anomaly on imaging studies, but one hypothesis is that the surface charge of the GNR interacted with proteins in the vitreous in a way that produced the opacity and may have played a role in the immune response. These charge-mediated interactions represent another barrier to using GNR to contrast-enhance OCT.

Additionally, GNR must be able to reach the tissue in which they are being designed to create contrast, in this case the retina. Delivery of relatively large GNR (~10x35nm) to the retina requires considering surface functionalizations that enhance their ability to penetrate retinal tissue in addition to animal models that may allow GNR delivery while maintaining clinical relevance.

The studies presented in this chapter represent our initial steps toward contrast-enhanced OCT. We establish that changes in GNR functionalization can improve the imaging potential of

GNR. We additionally probe how GNR might be delivered to the retina following intravitreal or intravenous injections. And we assess our ability to detect GNR in retinal tissue using OCT *in vivo*. And throughout this process, we strive to maintain the translational relevance of our studies as it relates to the contrast enhancement of OCT.

Methods

Gold Nanorod Surface Functionalization

Several GNR constructs are used in the experiments outlined in this chapter. Bare GNR with peak SPR of 808nm and a diameter of 10nm were purchased from a commercial source (A12-10-808; Nanopartz; Loveland, CO, USA), and these are referred to as "bare" or "CTAB-coated" GNR. This SPR peak is used for all GNR in the studies reported in this chapter because we theorized that this peak would maximally interact with the 800-900nm spectrum of the OCT system we use for imaging. These bare GNR were modified by sonication with polyethylene glycol-thiol constructs (Laysan Bio.; Arab, AL, USA) at a 10:1 molar overconcentration of PEG:CTAB for an hour to displace the CTAB with a PEG surface coating. In some cases the surface coating had an additional modified Tat peptide covalently bound to it. Tat is an HIV-surface peptide that enhances cellular uptake. Its sequence is RKKRRORRR. The products created following this displacement are called PEG-GNR or Tat-GNR, respectively.

Displacement of CTAB was confirmed via surface-assisted laser desorption-ionization time-of-flight mass spectrometry (SALDI-TOF-MS) (Voyager Elite; PerSeptive Biosystems; Framingham, MA, USA). SALDI uses the GNR surface to capture laser energy and generate unique ionized fragments determined by the composition of the GNR and its surface

functionalization[37]. SALDI of the GNR proceeded following calibration of the mass spectrometer with red phosphorous. All readings were taken in positive ion mode.

Figure 3a shows that SALDI of our bare GNR reports strong peak at 356 m/z caused by ionized gold-bromine particles, specifically of the form Au-Br_2, indicating the expected covalent bond between the nanoparticle gold surface and the bromine in CTAB. This result provides an efficient way to determine if residual CTAB remains on the GNR constructs. Figure 3b shows that our PEG polymer totally displaces CTAB on our PEG-GNRs.

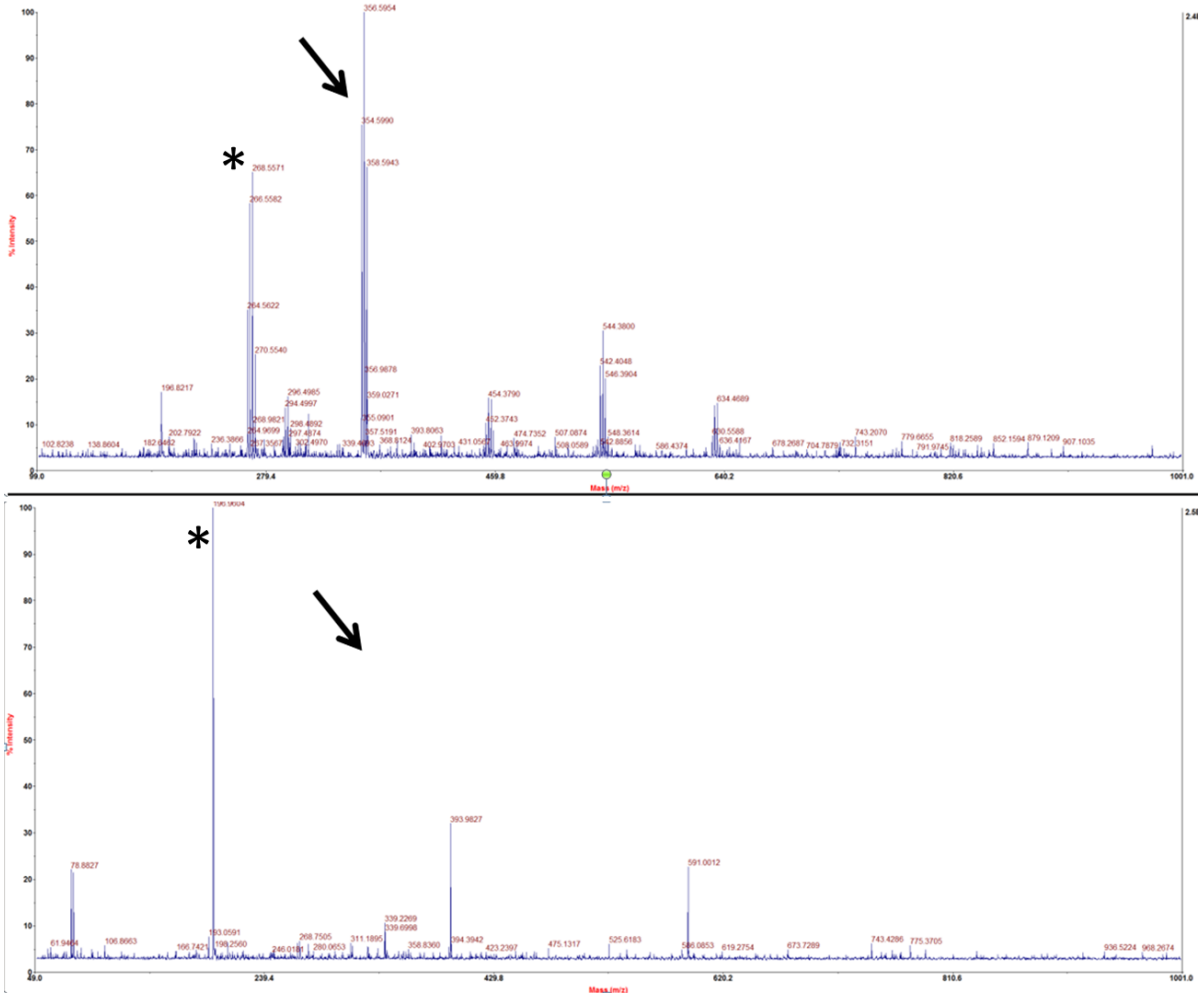

Figure 3: SALDI-MS of GNR Constructs. This figure shows the results of SALDI mass spectrometry run on bare GNR and PEG-GNR. (A) shows a large peak at 356m/z (arrow). This peak is associated with Au-BR_2, which is expected given the gold-bromine bond present on the surface of bare GNR. (B) demonstrates the loss of this peak (arrow) confirming displacement of surface CTAB in PEG-GNRs. (A,B) also demonstrate strong gold peaks near 197m/z (asterisks), which is expected when assaying GNR.

Additionally, GNR with a SPR of 808nm and a diameter of 10nm and a surface coating with a carboxyl moiety were purchased commercially (C12-10/750-TC-50; Nanopartz; Loveland, CO, USA). Surface functionalization of these GNR was achieved in a directed fashion using ethyl-3-(3-dimethylaminopropyl) carbodiimide (EDC) (Thermo Fisher Scientific; Waltham, MA, USA) crosslinking in the presence of N-hydroxysulfosuccinimide (sulfo-NHS) (Thermo Fisher Scientific, Waltham, MA, USA). The EDC coupling reaction allows the attachment of primary amine groups, such as those present on antibodies, to carboxyl moieties present on the surface of our GNR. The addition of sulfo-NHS to the reaction mixture improves the yield. We used two antibodies in this study. The first is a rat anti-ICAM2 antibody (Thermo Fisher Scientific, Waltham, MA, USA) which is our "targeted" antibody. ICAM2 is constitutively expressed on vascular endothelial cells. The second antibody is a rat IgG with no known reactivity to murine antigens (Thermo Fisher Scientific, Waltham, MA, USA) which is our control or "untargeted" antibody. The reaction proceeded via the addition of 10^{12} GNR to our reaction mixture followed by the addition of EDC and sulfo-NHS at 10-fold and 25-fold molar overconcentrations relative to surface carboxyl moieties in 1mL of deionized water. This mixture was allowed to react at room temperature for 2 hours with a magnetic stirring rod spinning at 60 rpm continuously mixing the solution. The GNR were then purified via centrifugation at 18,000g for 45 minutes followed by resuspension in deionized water. Following resuspension, either the targeted or untargeted antibody was added to the reaction mixture at 50-fold molar overconcentration relative to surface carboxyl moieties present on the GNR. This solution was allowed to react for an additional 2 hours at room temperature with a magnetic stirring rod spinning at 60 rpm to facilitate mixing. Following this reaction, antibody-functionalized GNR were purified by three rounds of centrifugation at 18,000g for 45 minutes followed by final

resuspension in isotonic phosphate-buffered saline (PBS) prior to intravenous injection. These purified GNR are referred to as "targeted" and "untargeted" GNR respectively. Unreacted antibody was retained and purified to assess for reaction yield via BCA assay, which was approximately 20 percent. Additionally, transmission electron microscopy was used to ensure that GNR size and morphology was unchanged by these reactions. Table 1 summarizes the GNR constructs we use in the studies in this chapter.

Name	Dia-SPR	Method	Functional Group
Bare GNR	10-808	As Purchased	CTAB
Peg-GNR	10-808	CTAB Displacement	PEG
Tat-GNR	10-808	CTAB Displacement	modTat
Untargeted GNR	10-808	EDC Crosslinking	IgG
Targeted GNR	10-808	EDC Crosslinking	ICAM2

Table 1: Summary of GNR Constructs Used in Experiments Reported in Chapter 2. This table lists the GNR constructs discussed in this chapter by their common name (Name), size and SPR peak in nm (Dia-SPR), method of surface functionalization (Method), and salient surface moiety (Functional Group). Note that CTAB displacement means surface CTAB was displaced by a thiol-linked PEG polymer.

Intravitreal and Intravenous GNR Injections

All animal treatments followed all requirements of the Vanderbilt University Institutional Animal Care and Use Committee and adhered to the Association for Research in Vision and Ophthalmology (ARVO) Statement for the Use of Animals in Ophthalmic and Vision Research. Wild-type (C57BL/6) mice aged 8-10 weeks were used in all experiments reported in this chapter. For all procedures including imaging, animals were anesthetized via the intraperitoneal injection of a drug mixture containing 13.2mg/ml ketamine and 1.5mg/ml xylazine in sterile water, with a total injected volume equal to 3.7mL/kg of animal body weight. For ocular procedures, GenTeal lubricant eye gel (Alcon, Hunenberg, Switzerland) was applied to the

cornea to prevent ocular dryness. Intravenous (tail-vein) and intravitreal injections were used to deliver GNR or appropriate controls, depending on the nature of the experiment being conducted. For tail-vein injections, 100uL of a GNR solution or PBS was injected 8 hours prior to any imaging being performed. Intravitreal GNR injections were performed ~3 minutes prior to imaging. Heating pads assisted in post-procedure recovery.

Laser-Induced Choroidal Neovascularization

The laser-induced choroidal neovascularization (LCNV) model was implemented with laser photocoagulation by a laser system (Carl Zeiss Meditec; Jena, Germany) with a laser (Coherence; Santa Clara, CA, USA) operating at 532nm and 120W pulsed for 0.1 seconds. The eye was manually manipulated to permit visualization of the mouse fundus as well as focusing of the laser on the RPE layer prior to firing. A microscope cover slide coupled to the eye with a 2.5% hydroxypropyl methylcellulose solution was used to aid in the operation. The spot size of the laser on the retina was 100 microns, and we attempted to place four lesions evenly spaced from one another, centered on the optic nerve head and approximately two optic disc diameters from it. We attempted to avoid damaging any major blood vessels with the laser, and any significant bleeding associated with the lasering process was noted and that lesion was excluded from further study. Lasering produces visible vapor bubbles following laser firing, which is a reliable indication that Bruch's membrane has been ruptured, which is necessary for implementing the LCNV model. Representative day 5 lesions were imaged via bright-light fundoscopy using the Micron IV imaging system (Pheonix Research Labs; Pleasanton, CA, USA).

Ex Vivo Immunohistochemistry and Imaging

Wild-type (C57BL/6) mice aged 8-10 weeks were treated in the LCNV model as previously described. Five days after lasering, the mice were intravenously injected with PBS, untargeted GNR, or targeted GNR. After allowing the GNR 8 hours to accumulate, the mice were anesthetized and enucleated. Their globes were fixed in 10% neutral buffered formalin (ThermoFisher Scientific; Waltham, MA, USA). The choroids were dissected from the surrounding tissue, washed with tris-buffered saline (TBS) (Corning Cell Gro; Corning; Corning, NY, USA), and blocked with 3% BSA in 0.1% Tween (Sigma-Aldrich; St. Louis, MO, USA) for 2 hours at room temperature. They were then stained with anti-Rat IgG antibody conjugated to Alexa Fluor 594 (A11007; Invitrogen; Waltham, MA, USA) and mounted with Prolong Gold with DAPI mounting media (P36942; ThermoFisher Scientific; Waltham, MA, USA). Following this treatment the choroids were imaged using an Eclipse-Ti microscope (Nikon; Melville, NY, USA).

In Vivo Optical Coherence Tomography

For all imaging done in this chapter, we used a commercial OCT system with a mouse retinal imaging lens operating in the 800nm-900nm range (Bioptigen, Inc.; Morrisville, NC, USA). Imaging data was acquired using 1000 A-scans/ B-scan and up to 100 B-scans for our largest retinal scans.

Results

Gold Nanorod Detoxification

For our first experimental attempt to visualize GNR using OCT, we injected bare GNR intravitreally and immediately imaged the result. Theoretically, GNR injected into the vitreous humor should be visible as small bright spots against the dark background of the vitreous, consistent with their strong scattering properties. However, previous studies published of similar injections shoed the formation of an amorphous opacity in the vitreous. As Figure 4 shows, we got a similar result following intravitreal injections of bare GNR. The opacity formed within minutes of injection and persisted for the duration of imaging, and obstructed the view of the retina. Figure 4 demonstrates the strong shadowing effect it has on the retina behind it. The image is also noteworthy for the lack of any punctate scattering effects we might expect from GNR.

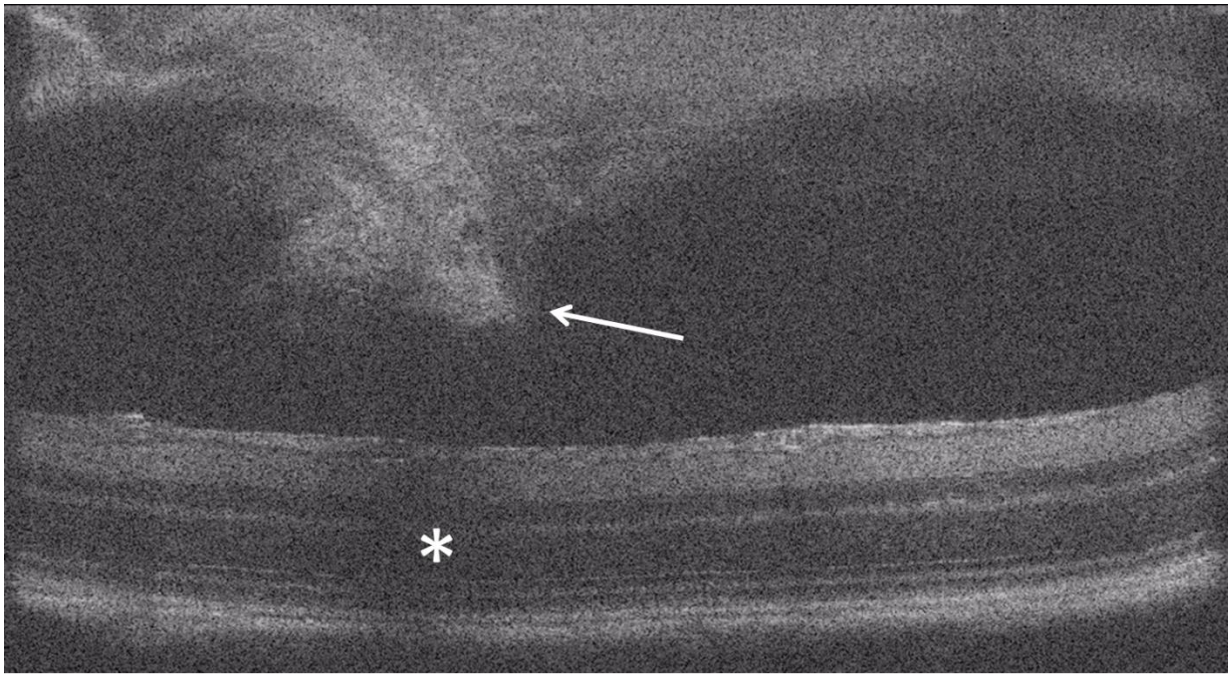

Figure 4: *In Vivo* Retinal Imaging Following Intravitreal Injection of Bare GNR. This image was acquired within minutes of bare GNR injection. It shows the formation of an amorphous opacity (arrow) throughout the vitreous. The opacity causes a considerable shadowing effect on the retina behind it (asterisk).

Given this strong and rapid interaction between the vitreous humor and the bare GNR, as well as the existing evidence for CTAB toxicity and stability issues, we opted to replace the CTAB with a steric inhibitor of aggregation, polyethylene glycol (PEG). PEG coating allows for GNR to maintain stability in solution, and should prevent the charge-mediated interaction between the GNR surface and surrounding proteins. Additionally, PEG is widely used to alter the properties of pharmaceutical compounds and is considered to be biocompatible[38].

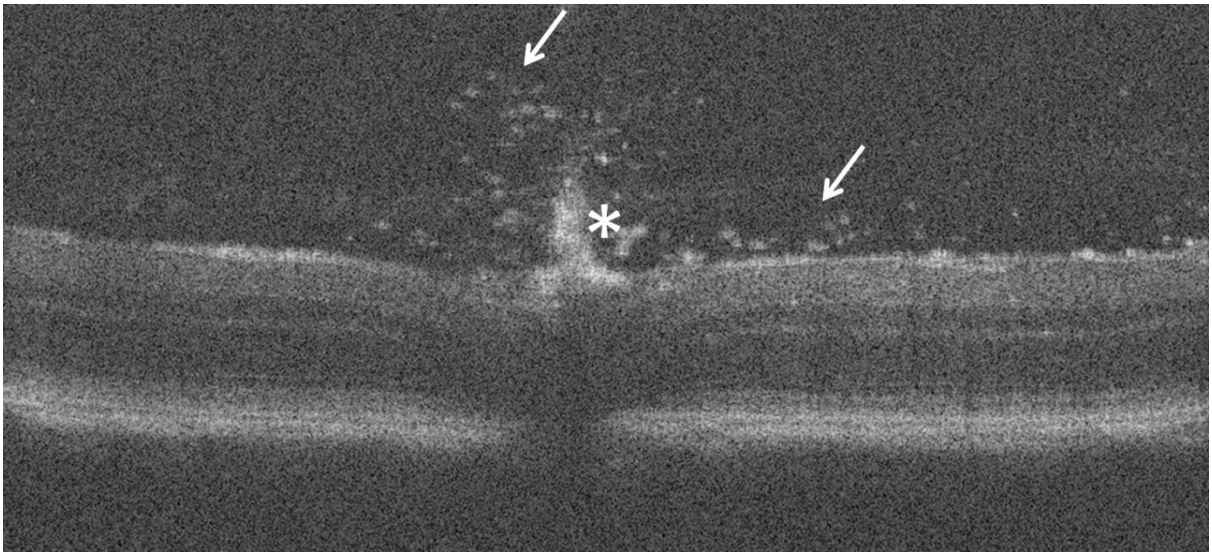

Figure 5: *In Vivo* Retinal Imaging Following Intravitreal Injection of PEG-GNR. As above, this image was acquired within minutes of the intravitreal injection of PEG-GNR. This image was taken through the middle of the eye and therefore shows the optic nerve head (asterisk). The presence of discrete scatterers (arrows) in the tissue is apparent near the inner retina extending into the vitreous. Of note, the amorphous mass and shadowing effects associated with bare GNR injections are not present here.

Figure 5 demonstrates that intravitreal injections of these PEG-GNR were successful in that they delivered GNR to the inner limiting membrane, plainly visible as punctate scatterers against the darkness of the vitreous humor. The size of these scatterers is larger than might be expected based on the size of GNR relative to the tissue being imaged, which might indicate some aggregation has occurred. The retina is plainly visible behind the PEG-GNR with no significant shadowing effects. This result is a step forward in terms of achieving surface

functionalization of GNR that is compatible with OCT imaging. However, as Figure 5 also shows, we could find no evidence that the PEG-GNR moved through the ILM into the retina, thus limiting their utility as retinal contrast agents. We attempted one more set of intravitreal injections with Tat-GNR, under the theory that the modTat surface peptide might promote intracellular uptake of the GNR through the ILM, but the results of the experiment with Tat-GNR were indistinguishable from those with PEG-GNR.

In Vivo Intravenous Gold Nanorod Delivery

In light of these mixed results with intravitreal injections, we decided to test the efficacy of intravenous GNR delivery to the retina via tail-vein injection. This change in delivery method presented several new challenges. The blood-retina barrier is generally not permeable to large molecular weight nanoparticles, which would make it difficult to get our GNR into the retinal tissue[39,40]. Also, it was unclear where these GNR might localize in the retina for our imaging purposes. If the GNR were widely dispersed, they might be difficult to detect on imaging.

To address these concerns, we chose to image our GNR in the laser-induced choroidal neovascularization, or LCNV, model[41]. This mouse model is often used as an acute approximation of "wet" or neovascular AMD, which allows our studies to maintain their translational relevance.[42,43] In LCNV, an ultraviolet-range laser is targeted to the RPE/Bruch's membrane layer of the outer retina. The energy from the laser is absorbed by the RPE and released as heat which severely damages Bruch's membrane. Where this laser injury occurs, endothelial cells and leaky vessels derived from the choroidal vasculature proliferate into the subretinal space, creating a lesion[44,45]. The morphology of this lesion changes over time. The lesion grows in size until the seventh day after the laser injury, when it plateaus and then begins

to spontaneously resolve[46]. This entire process can take several weeks. LCNV lesions are localized to the area surrounding the initial laser burn[47].

Due to the inflammatory milieu surrounding these lesions, there are a number of antibody-targetable surface ligands that are upregulated in in this animal model, the most important for our studies being CD102/ICAM2[48,49]. This biomarker is constitutively expressed on endothelial cells, and almost all LCNV lesions contain increased numbers of endothelial cells[50]. Using this model in our studies has many potential benefits. It weakens the blood-retinal barrier to allow the accumulation of large nanoparticles in a way that still maintains the translational relevance of the studies. It also provides a visible, localized area where GNR would be expected to accumulate both passively and due to potential targeting effects.

Figure 6 shows a fundoscopy image taken five days after treatment in the LCNV model. The lesions are plainly visible and localized to the area surrounding the laser burn. Some blood is also visible in the upper left quadrant, which is a possible side effect of lasering. In our experiments in the LCNV model, we wanted to assess the ability of GNR to accumulate in the laser lesions, and in particular we wanted to assess the potential of GNR surface functionalization to generate a targeted effect in the LCNV model. Mice were treated in the LCNV model, and on day 5 post-lasering, they were tail-vein injected with PBS, untargeted, or targeted GNR. We gave the GNR 8 hours to accumulate in the lesions, and then isolated the choroids. The choroids were stained with a DAPI nuclear stain and an Alexa Fluor 594-conjugatee anti-rat-IgG antibody prior to flat mounting. The only potential sources of rat IgG in these mouse choroids were the antibodies covalently bound to the surface of the injected GNR. Essentially, we used our intravenously injected GNR as primary antibody for an immunohistochemical study in order to assess GNR delivery.

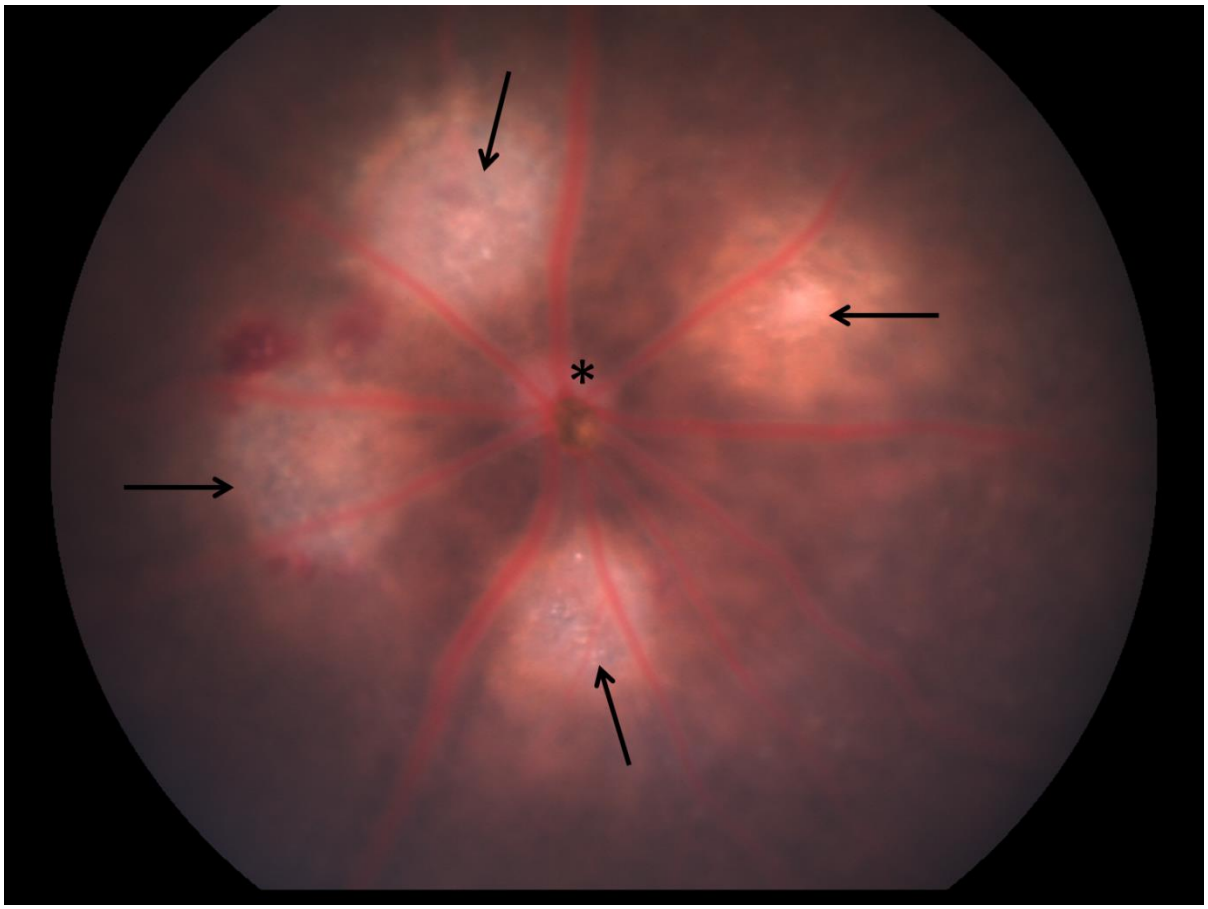

Figure 6: *In Vivo* Bright-Light Fundoscopy of Mouse Retina Treated in LCNV Model. This is a representative image of a mouse retina treated in the LCNV model take five days after lasering. The optic nerve head (asterisk) is visible and surrounded by blood vessels radiating away from it. The four laser injuries (arrows) are evenly spaced about the optic nerve head. Note the presence of red blood on the left half of the image.

Figure 7a-c shows that all of the lesions stain with DAPI nuclear stain. Since all LCNV lesions involve the proliferation of cells, the DAPI results are as expected. Figure 7f shows that the strongest anti-rat IgG staining occurs in the mouse injected with targeted GNR. There is still some anti-rat-IgG staining in the lesion of the mouse injected with untargeted GNR (7e), and there is virtually none in the lesion of the PBS-injected mouse (7d). While this is not a quantitative study, it does demonstrate that there is a qualitative increase in GNR accumulation in LCNV lesions following the injection of untargeted GNR and particularly targeted GNR. This piece of data alone is not proof of retinal GNR delivery or a targeting effect. However, it did

inform our decision to pursue *in vivo* retinal imaging of intravenously injected GNR using OCT using the LCNV model.

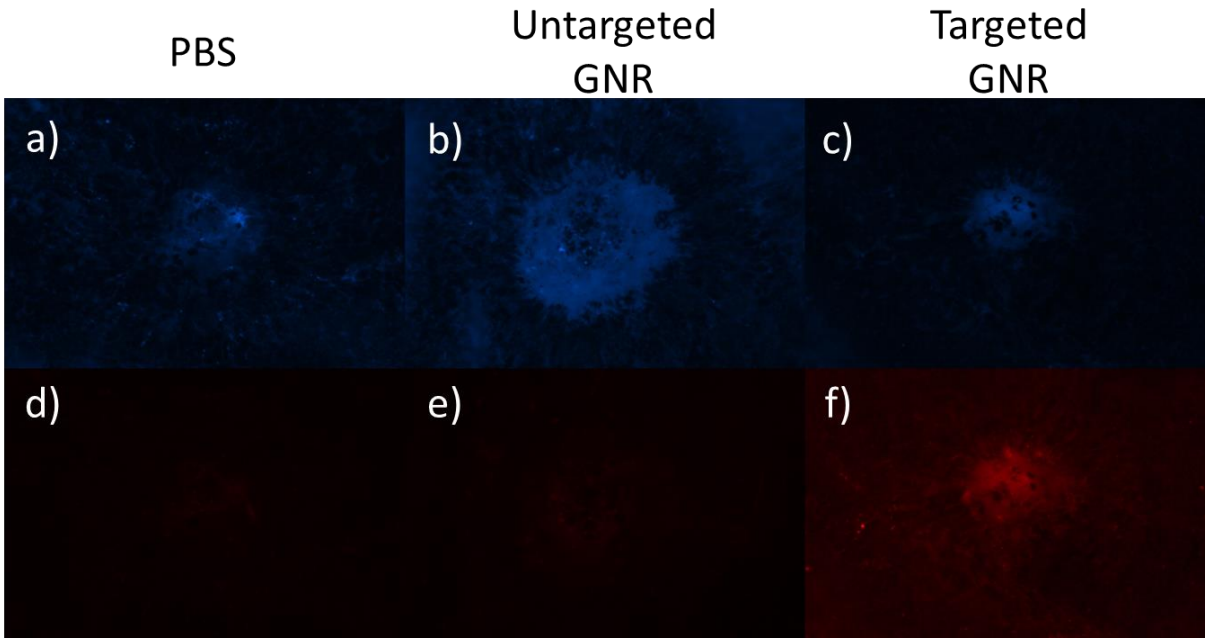

Figure 7: *Ex Vivo* Flatmounts of Stained Mouse Choroids Treated in the LCNV Model Following GNR Injection. Each paired column represents a single LCNV lesion treated with a DAPI nuclear stain (A,B,C) and an anti-rat IgG antibody conjugated to an AlexaFluor 495 fluorophore (D,E,F). (A,D) show a representative lesion from a mouse injected with PBS. (B,E) show a lesion of a mouse injected with untargeted GNR. (C,F) show a lesion of a mouse injected with targeted GNR. All three lesions show DAPI staining, but the strongest anti-rat-IgG counterstaining is present in the lesion from the mouse injected with targeted GNR.

In Vivo OCT Imaging of Intravenously Delivered GNR

After the successful *ex vivo* result, we sought to assess whether these GNR constructs would be visible on standard OCT imaging *in vivo*. We initiated a pilot study that followed the same design as the previous *ex vivo* study, with mice injected on day-5 post-lasering with PBS (n=10 eyes) or targeted GNR (n=10 eyes) and imaged at 8, 24, and 48 hour post-injection time points. Laser lesions were imaged and assessed for the presence of visible scatterers or detectible

large-scale changes in light reflection and absorption that would be consistent with GNR accumulation.

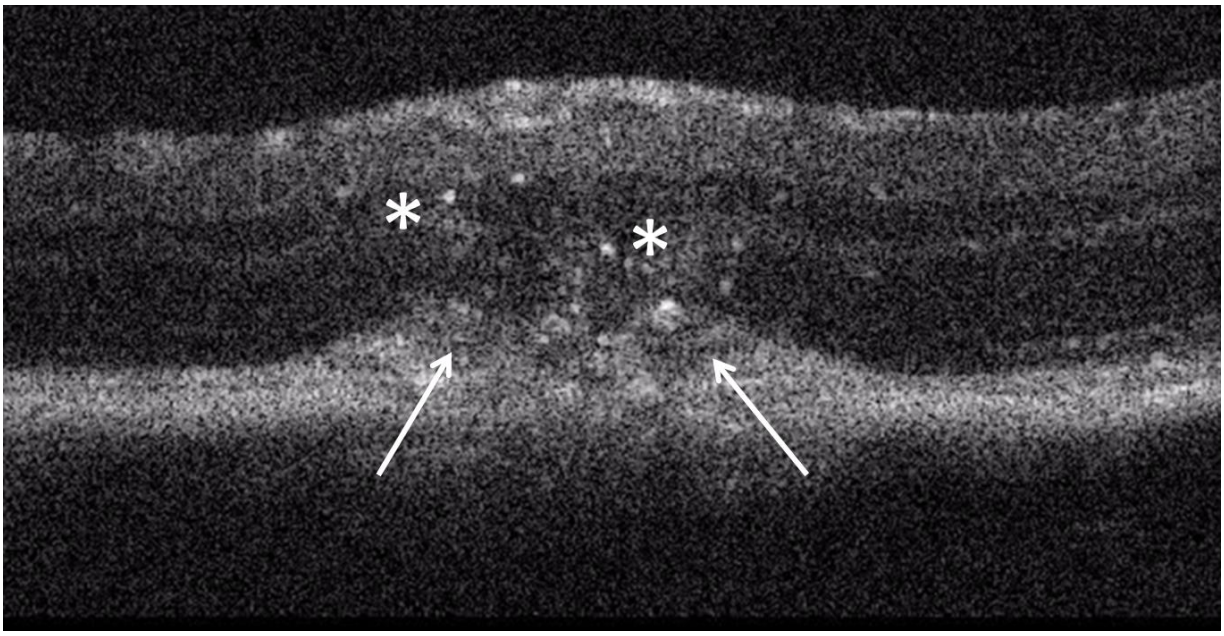

Figure 8: *In Vivo* OCT Imaging of the Retina of a Mouse Treated in the LCNV Model Following Intravenous PBS Injection. This is a representative image of a day-5 LCNV lesion in the mouse retina imaged 8 hours after intravenous PBS injection. It demonstrates a large morphological change extending from the choroid into the retinal space (arrows) with endogenous punctate scatterers present as well (asterisks).

Figure 8 shows a typical day 5 LCNV lesion imaged natively by an OCT system, 8 hours after PBS injection. There are a number of changes in the degree of reflectivity across the tissue due presumably to the agglomeration of cells and other biological detritus following laser injury. The image demonstrates that there is already a high degree of heterogeneous scattering occurring even without GNR injections, which will complicate GNR detection. In fact, the punctate scattering shown in Figure 6 is similar to that associated with GNR injection in Figure 4 (intravitreal PEG-GNR injection), although there are no GNR present in Figure 6.

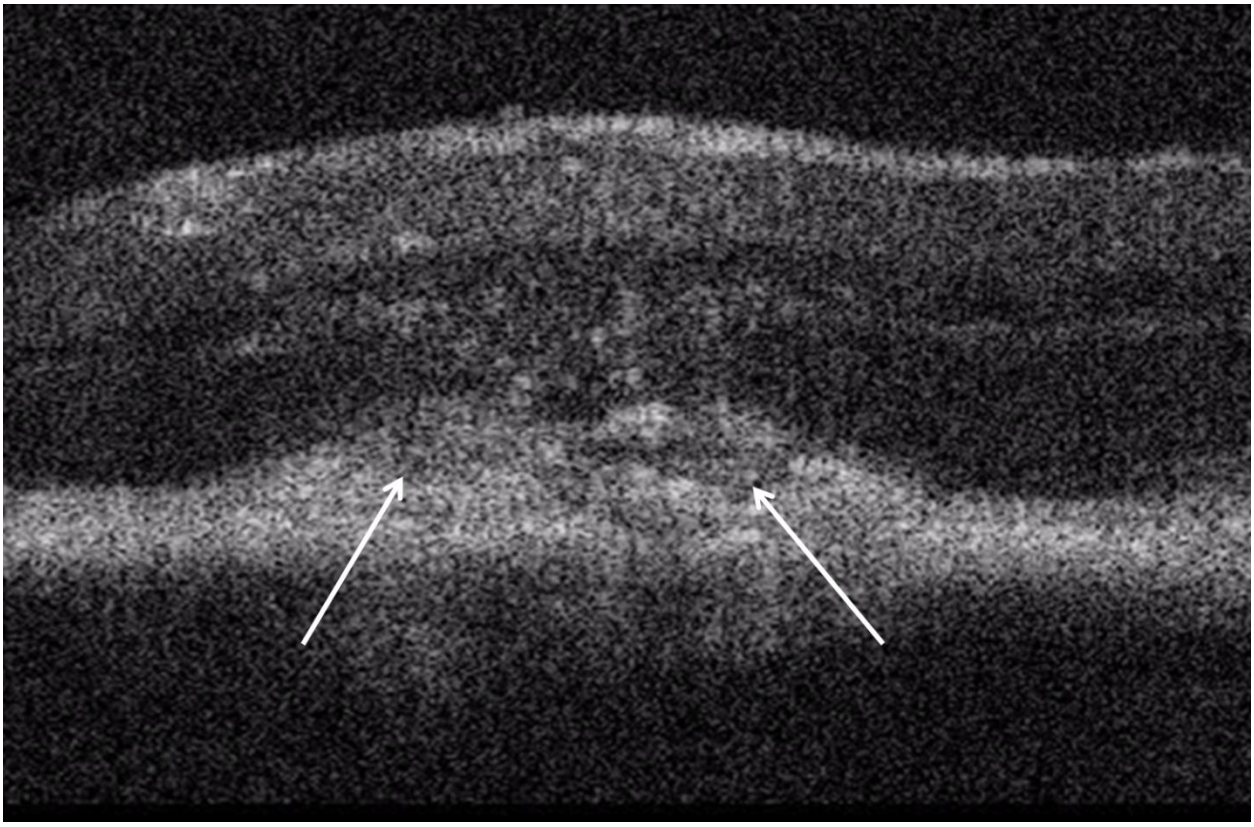

Figure 9: *In Vivo* OCT Imaging of the Retina of a Mouse Treated in the LCNV Model Following Intravenous Targeted GNR Injection. This is a representative image of an LCNV lesion in the mouse retina acquired by OCT five days after lasering and 8 hours after the intravenous injection of targeted GNR. As in Figure 6, there is a characteristic morphological change in the outer retina (arrows). But this image is most noteworthy for the lack of any detectable changes due to the GNR injections.

Figure 9 shows a day-5 lesion on OCT imaged 8 hours after the injection of targeted GNR. There is no discernible difference in the degree of tissue reflectivity either in totality or in texture associated with GNR injection. There were also no changes in overall absorption that we were able to measure. While many of the *in vivo* images presented in this chapter were taken as part of larger studies, the imaging results were not quantified e.g. in terms of lesion brightness. This quantification was not performed because it was unclear from the images what changes might have occurred due to GNR accumulation or where they might be localized. In short, since we could not see any changes to quantify, quantitative analysis was not indicated. These results

suggest that the scattering caused by GNR becomes very difficult to detect in the heterogeneously scattering environment of the retina, particularly in an LCNV lesion.

Discussion

On a positive note, the studies reported in this chapter show us developing tools that got us closer to our goal of contrast-enhanced OCT, but we also report the setback of being unable to successfully image GNR in the retina *in vivo*. We demonstrate that we could effectively and totally displace the CTAB present on the surface of "bare" gold nanorods with PEG, and that this significantly improved the properties of the GNR as an imaging adjuvant. The impressive benefit of novel surface functionalizations, particularly those involving PEG, to the performance of GNR became clear with these studies. Further, we developed chemical approaches to modify surface PEG by covalently attaching various uptake- and target- altering proteins.

We demonstrate that we can inject GNR intravitreally and intravenously, and that we can image retinal tissue following these injections *in vivo*. This is a major step forward in OCT imaging of GNR, because there was concern that the visually obstructive reaction to bare GNR in the vitreous previously published would preclude the use of GNR as a source of contrast in retinal studies[36].

This effect of bare GNR on the vitreous is interesting in its own right. Previous work showing a similar visual effect also provides evidence that these GNR are immunogenic, so it was assumed that the immune system was responsible for the optical effect[36]. However, the speed of this effect suggests that it might not be mediated entirely by the immune system per se, although CTAB is toxic to cells and it has a clear role. We were able to assess the speed of this effect because we could image our animals within minutes of the intravitreal injections, while the

previous study waited ten times longer between injection and imaging, at minimum. Given its immediacy, this opacity could be the result of a charge-mediated interaction between the GNR surface and the proteins present in the vitreous, although it could also be due to GNR internalization by immune cells, or some combination of these and other effects. Clarifying the exact nature of this effect would require further study.

We additionally determined that LCNV was a viable animal model for studying and imaging GNR delivery. Our immunohistochemical staining of flat mounted choroids, while imperfect, suggested that GNR were being delivered to LCNV lesions in the retina, and that a targeting effect due to surface antibody selection was present as well. However, it became apparent that while we may be able to deliver GNR to LCNV lesions, we could not readily detect them using OCT due to the background noise caused by the heterogeneous retinal and choroidal tissue present in the laser lesions. This obstacle suggested that in order to achieve retinal imaging of GNR and thus contrast-enhanced OCT, we would need to rely on OCT imaging adjuncts capable of detecting targeted gold nanorods despite this background noise.

Chapter 3: *In Vivo* Imaging of GNR Using Photothermal Optical Coherence Tomography

Introduction

In the previous chapter we demonstrate that it is possible to construct and modify GNR to make them more amenable to imaging using OCT. However, we also show that standard OCT systems have great difficulty imaging GNR in the heterogeneously scattering tissue of the retina, which is one of our major goals. In this chapter, we address this deficiency by using photothermal OCT (PT-OCT) in combination with GNR for *in vivo* retinal imaging.

As discussed in the background section of chapter 1, PT-OCT operates by using a laser source separate from the one used to generate the OCT image to heat whatever absorbers are present in the tissue being imaged[28]. These absorbers can be endogenous, as in the case of melanin in the RPE, or exogenous, as in the case of intravenously injected GNR[16]. The degree of heating in the tissue is variable, but is in the range of 1-3 degrees Celcius[51]. This degree of temperature increase is unlikely to cause any damage to ocular tissues, and no gross morphological changes due to PT-OCT heating were observed during our studies. Heating these absorbers ultimately changes the optical path length (OPL) of light passing through the surrounding media, which can be detected in the data collected by standard OCT systems[51]. The PT signal is reported as the magnitude of the change in optical path length in nanometers.

Once again, GNR are a useful adjuvant for an OCT imaging adjunct, in this case because they are excellent light absorbers and their absorption peaks can be tuned to sit at the wavelength emitted by the PT source light[21]. This is an important aspect of the studies discussed in this chapter, as here we use GNR with absorption peaks tuned to the photothermal laser source at 750nm rather than tuned to the OCT light source as in the previous chapter's studies. The use of

GNR with PT-OCT has been previously demonstrated, although it has never before been demonstrated in the eye or more specifically for our research, the retina.

To generate an appropriate target for our imaging studies in the mouse retina *in vivo*, we will again use the LCNV model in the mouse. As described in the previous chapter, this mouse model is often used as an acute approximation of "wet" or neovascular AMD[42]. It has the advantage of presenting a localized target for our photothermal imaging in addition to having abnormal vasculature that might serve to concentrate GNR in the lesions.

In this chapter, we demonstrate the ability of PT-OCT technology to achieve *in vivo* retinal imaging of both endogenous (RPE melanin) and exogenous (GNR) contrast agents in the LCNV model. Additionally, we demonstrate the utility of PT-OCT detection of molecularly targeted GNR to generate high-resolution contrast-enhanced images physiological changes in the retina. To accomplish these goals, we first image wild-type and albino mice show that melanin is an endogenous PT-OCT contrast agent present in the mouse retina. Then we use PT-OCT to image mice treated in the LCNV model after intravenously injecting them with ICAM2-targeted GNR to assess our ability to detect these GNR *in vivo* over the melanin background signal. We use injections of untargeted GNR or PBS as controls for these experiments. In comparing the lesion-associated photothermal signal from these cohorts we can assess our ability to detect targeted exogenous contrast agents in the mouse retina using PT-OCT.

The other question we consider in this chapter is whether PT-OCT imaging of GNR allows for the detection of clinically relevant physiological changes in the mouse retina *in vivo*. To model a clinically relevant change, we use the standard LCNV model as before, but in one eye of each mouse we inject anti-VEGF antibody, while in the other eye we inject PBS. VEGF signaling is a major driver of neovascularization in LCNV lesions, so we anticipate anti-VEGF

treatment to reduce the proliferation of neovascular endothelial cells in the lesions, thereby reducing lesion volume as well as the concentration of ICAM2-targeted GNR that will accumulate in these lesions[52–55]. Additionally, anti-VEGF treatments are a very common clinical therapeutic intervention in patients with wet AMD (which we model with LCNV), maintaining the translational relevance of this experiment. In assessing our ability to detect anti-VEGF-induced changes to LCNV lesions *in vivo,* we are assessing the utility of PT-OCT imaging of GNR to detect clinically relevant physiological changes in the retina, which is one of our major goals with this research. The imaging of endogenous retinal melanin, the imaging of molecularly targeted GNR, and the detection of non-structural changes in LCNV lesions *in vivo* are all novel applications of PT-OCT technology.

The work discussed in this chapter was performed as a collaborative effort. The studies discussed in this chapter have already been published either in Lapierre-Landry et al. (Sci. Rep., 2017) or Gordon et al. (Trans. Vis. Sci. Tech., In Press)[16,56]. The figures and captions (modified in some cases) in this chapter are reprinted with permission from those authors.

Methods

Gold Nanorod Functionalization

The GNR used in the studies reported in this chapter have dimensions of 10nm by 35nm, with peak absorption at 750nm. Aside from this change, GNR functionalization proceeded as described in chapter 2. We used the same two antibodies in this study as in the previous chapter. The first is a rat anti-ICAM2 antibody (Thermo Fisher Scientific, Waltham, MA, USA) which is our "targeted" antibody. The second antibody is a rat IgG with no known reactivity to murine antigens (Thermo Fisher Scientific, Waltham, MA, USA) which is our control or "untargeted"

antibody. The resulting GNR constructs are referred to as untargeted GNR and targeted GNR respectively.

Animal Treatments, Drug and Contrast Agent Delivery, Lasering, and Imaging

All animal treatments followed all requirements of the Vanderbilt University Institutional Animal Care and Use Committee and adhered to the Association for Research in Vision and Ophthalmology (ARVO) Statement for the Use of Animals in Ophthalmic and Vision Research. Male albino (BALB/c) and wild-type (C57BL/6) mice aged 8-10 weeks were used in all experiments reported in this chapter. For all imaging procedures, animals were anesthetized using continuous isoflurane administration (2-5%) in air either in a box or via nose cone. For procedures involving laser photocoagulation or injections (tail-vein or intravitreal), animals were anesthetized via the intraperitoneal injection of a drug mixture containing 13.2mg/ml ketamine and 1.5mg/ml xylazine in sterile water, with a total injected volume equal to 3.7mL/kg of animal body weight. For procedures involving the eye, GenTeal lubricant eye gel (Alcon, Hunenberg, Switzerland) was applied to the cornea to prevent ocular dryness. Regardless of the type of anesthesia or procedure performed, mice recovered on heating blankets until they were awake and behaving normally.

All other injections were either intravenous or intravitreal. Intravenous tail-vein injections were used to deliver GNR or appropriate controls, while intravitreal injections were used to deliver anti-VEGF treatments or appropriate controls. For the tail-vein injections, 100uL of a GNR solution or PBS was injected 8 hours prior to any imaging being performed. Intravitreal injections were accomplished by the insertion of a small-guage needle through the mouse cornea behind the lens followed by the injection of either 2uL of anti-VEGF antibody

solution (AF-493-NA; R&D Systems; Minneapolis, MN, USA) in one eye of a mouse, with a PBS injection into the contralateral eye serving as an intravitreal injection control. Intravitreal injections were performed immediately following lasering.

The laser-induced choroidal neovascularization (LCNV) model was implemented with laser photocoagulation by a laser system (Carl Zeiss Meditec; Jena, Germany) with a laser (Coherence; Santa Clara, CA, USA) operating at 532nm and 120W pulsed for 0.1 seconds, using the same procedure outlined in chapter 2. Representative day 5 lesions were imaged via bright-light fundoscopy using the Micron IV imaging system (Pheonix Research Labs; Pleasanton, CA, USA) and via optical coherence tomography using our modified spectral-domain OCT system (Leica Microsystems Inc.; Buffalo Grove, IL, USA).

For mice treated in the LCNV model, all imaging was done 5 days following laser photocoagulation, a time point chosen because it allows for the presence of vascular endothelial cells in the lesion without as significant a presence of RPE cells, which produce endogenous photothermal contrast that we sought to minimize[47]. This is demonstrated in Figure 10. Figure 10b shows that the LCNV lesion itself has very few RPE cells in it on day 5 post-lasering, while Figure 10a demonstrates how this finding appears on OCT. For our albino vs wild-type PT-OCT studies, 6 eyes were imaged from 3 mice in each cohort. For our three-arm study of imaging GNR delivered to LCNV lesions, the PBS control arm had 21 eyes imaged, while the two GNR injected arms (targeted and untargeted GNR) had 14 eyes each. The study assessing the effects of anti-VEGF treatment on PT-OCT imaging of targeted GNR in lesions used 14 eyes from 7 mice for a paired analysis.

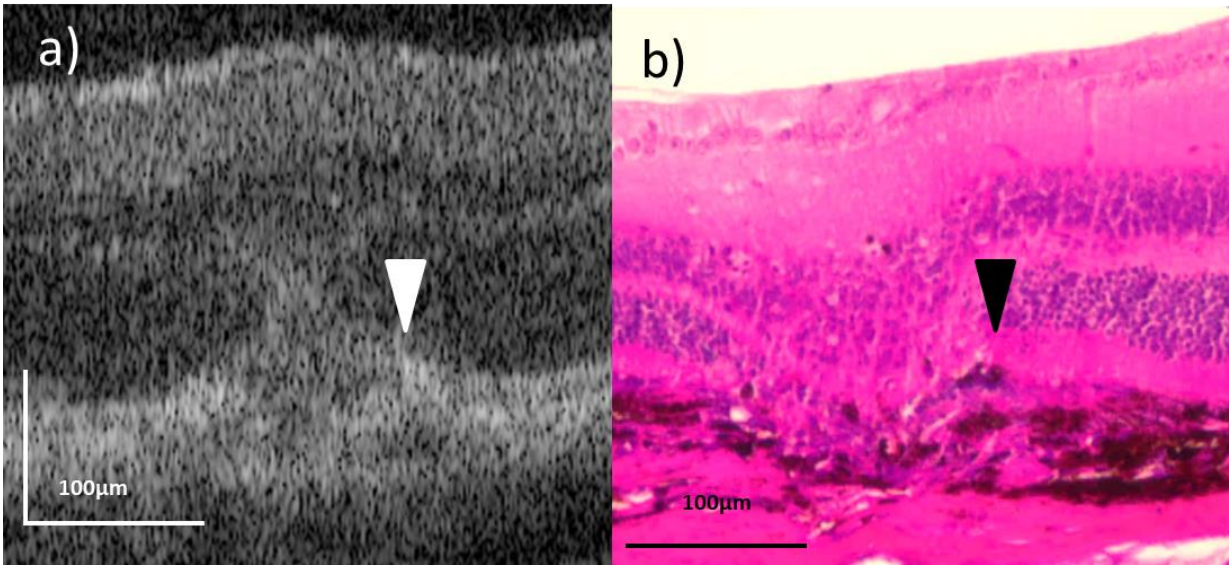

Figure 10: Comparison of Day 5 LCNV Lesions using OCT. (a,b) show representative OCT *in vivo* and H&E *ex vivo* images of day 5 LCNV lesions. The RPE (white and black arrowheads, respectively) is visibly disrupted.

Instrumentation, Signal Analysis, and Image Correction

For all imaging done in this chapter, we use a spectral domain OCT system (Leica Microsystems Inc.; Buffalo Grove, IL, USA) that was modified for PT-OCT imaging. The OCT system's broadband light source was centered at 860nm (40nm bandwith), and the photothermal laser was centered at 750nm. The photothermal (PT) laser had a power of 8mW for all experiments discussed here and was amplitude modulated via an acousto-optic modulator (Brimrose; Sparks, MD, USA) at f0=500Hz (50% duty-cycle, square wave). The modified system repeated 700 A-scans (M-scans) in a given location to help derive a photothermal signal, and repeated this process 400 times to construct a B-scan (400 A-scans/B-scan). The data collected by the system was used to generate the photothermal signal, expressed as the change in optical path length in nanometers in the tissue due to heating caused by the photothermal laser source. Images were corrected for breathing artifacts common in live-animal retinal imaging using an algorithm from Guizar-Sicairos et al[57]. A thorough explanation of the data processing

required to isolate a photothermal signal from raw OCT interferogram data is available in Lapierre-Landry et al. (Sci. Rep., 2017)[16].

After deriving the photothermal signal from the raw data, the images were analyzed by hand-selecting the region of interest (ROI) corresponding to the extent of the LCNV lesion visible on a given B-scan. These selections were made to include the LCNV lesion while excluding the RPE layer, as this layer contains melanin that produces a strong photothermal signal. This selection was made while blinded to the photothermal signal associated with the lesion, which was our primary experimental endpoint. After making these selections for every B-scan associated with a given lesion, those measurements were combined to create the overall lesion volume. These volumes were then used to calculate both a lesion size and total photothermal signal, from which average photothermal signal density can be derived by dividing photothermal signal by lesion volume. Exclusion criteria for a lesion from these studies included severely abnormal morphology, notably retinal detachment. Additionally, individual B-scans from a lesion volume were excluded if poor image quality prevented photothermal measurements to be taken, most commonly due to corneal opacities or the presence of gross blood in or near the retina.

Further imaging was performed using the modified OCT system but without using the additional photothermal laser source. These images were used to estimate the size of LCNV lesions by measuring the lesion size on the B-scan with the maximal extent of the measured area of the associated LCNV lesion. This single B-scan lesion measurement is called a lesion diameter.

Significance Tests

For the experiment comparing pigmented to albino mice, the differences between the two groups were assessed using the Mann-Whitney U test, which was used because the low number of samples necessitated a non-parametric statistical test. For the three-armed control/untargeted/targeted GNR experiment, a cluster analysis was performed in consultation with the Vanderbilt Biostatistics Department to determine the statistical significance of differences in the means the cohorts. A Tukey analysis was performed following estimations of statistical fixed effects between the three cohorts using a linear mixed effect model. This more complex statistical analysis was necessary because one or two eyes from a given mouse could have been used as part of the experimental cohort, and a for a given mouse both eyes were subject to the same tail-vein injection, meaning they cannot be treated as independent for experimental purposes. The final set of experiments involving paired anti-VEGF/PBS injections into different eyes of the same mouse was analyzed for statistical significance using a one-tailed Wilcoxon signed-rank analysis assessing differences in lesion-associated photothermal signal density, as well as in lesion size. This test was appropriate because of the paired nature of the experiments. In all cases a p-value ≤ 0.05 was considered significant.

Results

In Vivo Retinal Imaging of Albino and Wild-Type Mice Using PT-OCT

Melanin is a known absorber of light across a broad spectrum, including the wavelength used by our photothermal laser source. In order to determine the extent to which melanin-associated PT signals were detectable using *in vivo* imaging, the retinas of untreated BALB/c albino mice (n=6 eyes) and C57BL/6 mice (n=6 eyes) were imaged using our PT-OCT system.

The results are reported as a photothermal signal density across the entire image, rather than that associated with a lesion.

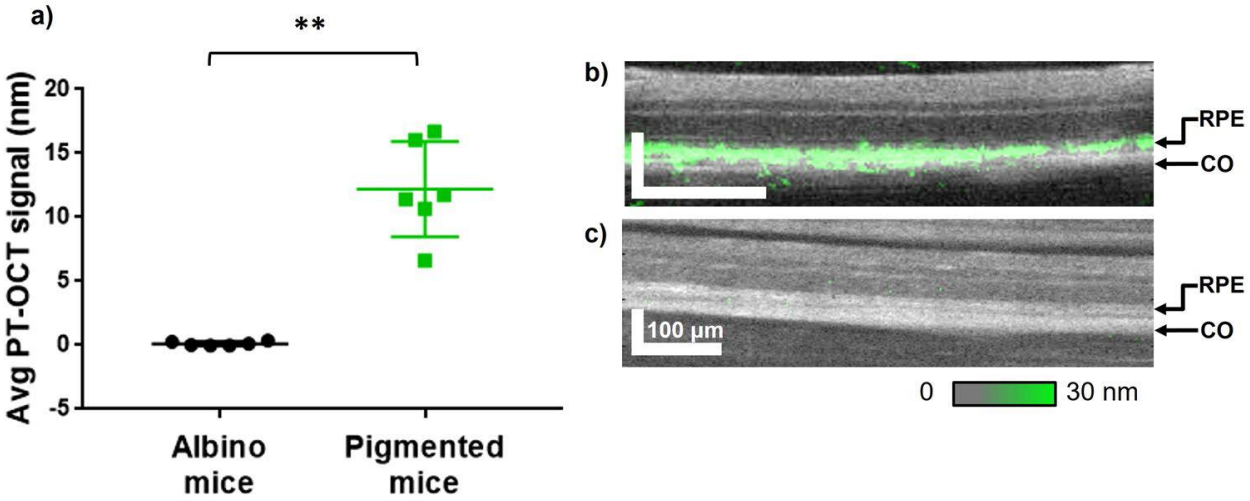

Figure 11: *In Vivo* PT-OCT Imaging of Albino and Wild-Type Mouse Retinas. (A) Average retinal PTOCT signal for albino and wild-type mice, with error bars representing standard deviation. There is a significant increase in PT-OCT signal in the wild-type mice, with almost no signal present in the albino mice; **p≤0.01. (B,C) show representative images from wild-type and albino mice, respectively, with a green PT-OCT overlay. Legend: RPE (retinal pigmented epithelium), CO (choroid). This figure is reprinted here with permission of the authors from Lapierre-Landry et al. (Sci. Rep., 2017).

Figure 11a shows there is virtually no detectable photothermal signal in any of the images of the retinas of albino mice, while there is considerable photothermal signal present in all of the retinas of wild-type mice. This is a statistically significant difference. Representative B-scans of retinas including a green photothermal signal overlay from the two cohorts are shown in Figure 11b,c.

In Vivo Retinal Imaging of GNR in the LCNV Model Using PT-OCT

Following our successful detection of endogenous photothermal contrast in the mouse retina, we assess our ability to detect and evaluate exogenous contrast agents *in vivo*. C57BL/6 mice were treated in the LCNV model. On day 5 post-lasering, the mice were tail-vein injected

with PBS, untargeted GNR, or targeted GNR. The targeted GNR were functionalized with anti-ICAM2 antibody. 8 hours following the tail-vein injections, laser lesions from mice in each experimental group were selected and imaged and the lesions' photothermal signal density was calculated. For the untargeted GNR cohort, photothermal signal density above baseline was used to assess the degree of passive accumulation of GNR in laser lesions. In the targeted cohort, the measurements assessed GNR accumulation for a targeting effect.

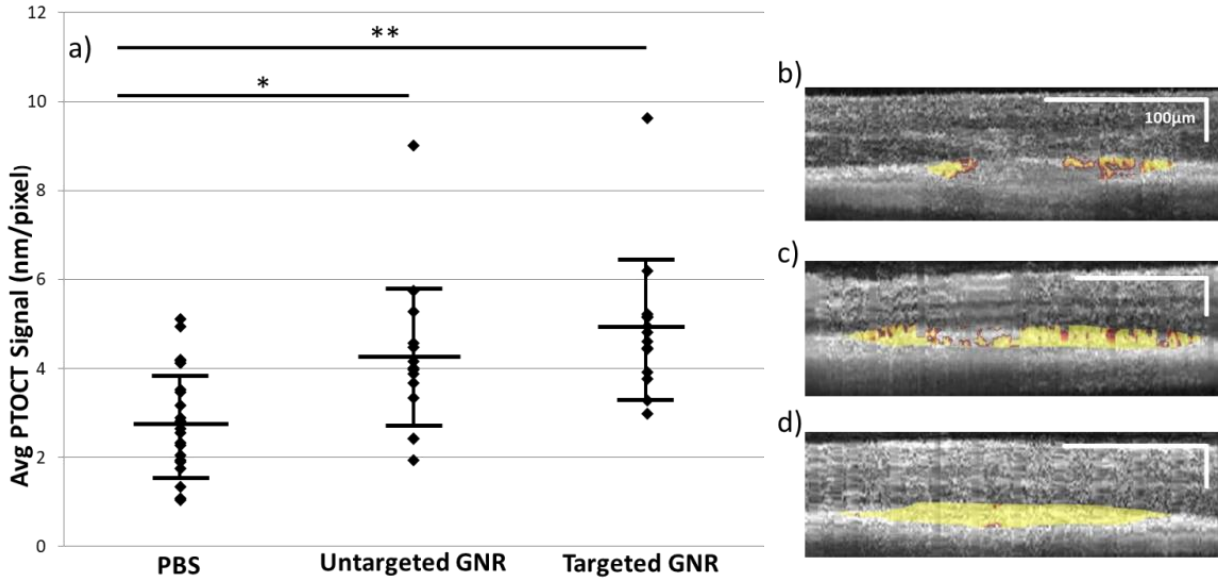

Figure 12: PTOCT of Untargeted and Targeted GNR *In Vivo*. (a) Average PTOCT signal density for each cohort, with error bars representing standard error of the mean. There is a significant increase in this signal associated with both untargeted and targeted GNR injections versus PBS control. *p≤0.05; **p≤0.001. (b-d) representative OCT B-scans of mice injected with PBS (b; n=21 eyes), untargeted GNR (c; n=14 eyes), and targeted GNR (d; n=14 eyes) respectively, with lesion-associated photothermal signal overlaid in gold. Note the increased concentration of photothermal signal associated with passive accumulation of GNR in the lesions, and the greater increase associated with the injection of targeted GNR.

The results from the three cohorts are reported in Figure 12a as photothermal signal density in laser lesions for each of the three experimental cohorts. In mice injected with PBS, there was an average photothermal density of 2.82 nm/pixel (+/- 1.20 nm/pixel standard deviation, n=21 eyes), which is our minimum possible photothermal density measurement due to

melanin-induced background photothermal signal. The photothermal signal density in the untargeted GNR cohort (4.20 +/- 1.74 nm/pixel, n=14) is 1.49 times higher than in the PBS cohort, a statistically significant difference. The signal density in the targeted GNR cohort (4.89 +/- 1.60 nm/pixel, n=14) was stronger still, at 1.73 times higher than background noise. While the difference between the targeted GNR and PBS cohorts is statistically significant, the difference between the targeted GNR and untargeted GNR cohorts is not, although there is a trend toward more signal from the targeted GNR. Representative B-scans of laser lesions with associated photothermal signal overlaid in gold from the three cohorts are shown in panels 12(b-d).

PT-OCT Imaging of Targeted GNR Accumulation After Anti-VEGF Injection in the LCNV Model

One of the major goals of this research is to create tools that allow us to expand the purview of OCT beyond its current realm of structural imaging to allow the imaging of physiological changes *in vivo*. To accomplish this goal using PT-OCT and GNR technology, we treated wild-type mice in the LCNV model. Immediately following lasering, the mice were given an anti-VEGF treatment or a PBS control via intravitreal injection. The anti-VEGF compound was an anti-mouse-VEGF neutralizing antibody, and its presence in the retina should down-regulate VEGF signaling and thus the extent of choroidal neovascularization and ICAM2 expression in laser lesions[50,52]. On day 5 post-lasering (and post-intravitreal injection), mice were tail-vein injected with targeted GNR, as in the previous experiment. PT-OCT imaging of lesions was performed 8 hours after the tail-vein injections, and photothermal signal density of lesions from the anti-VEGF-injected and PBS-injected eyes were measured and compared.

We confirmed the efficacy of the anti-VEGF injections by demonstrating their ability to reduce the size of laser lesions as predicted. Lesion diameters for both the anti-VEGF and PBS cohorts (n=7 paired eyes in each cohort) are reported in Figure 13a, which shows that in every mouse, the anti-VEGF injected eye had a smaller lesion than the PBS-injected eye, which is a statistically significant difference. This result confirms that the anti-VEGF injections were having their intended physiological effects in this set of experiments, which would include decreased lesion volume, endothelial cell concentration, and vascular leakiness. Figure 13b-c shows representative OCT B-scans from each cohort.

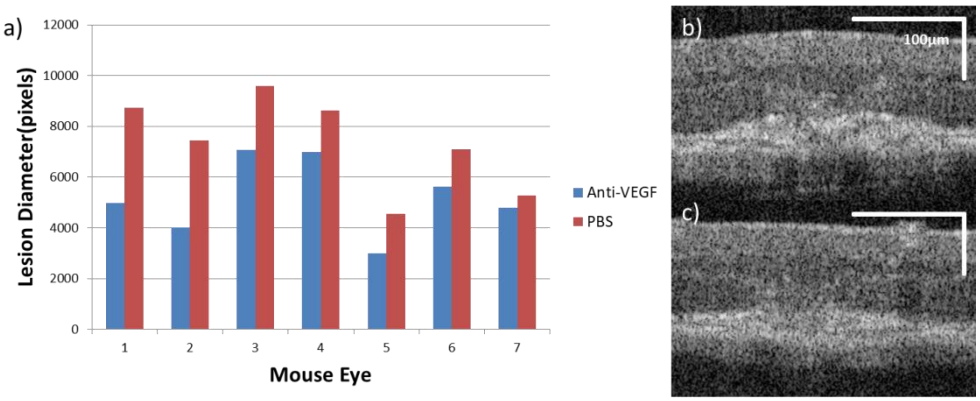

Figure 13: Estimates of Lesion Size With or Without Intravitreal Anti-VEGF Injection *In Vivo*. (a) shows the lesion diameter from every eye in both experimental cohorts, paired by mouse (n=7 mice). The results are ordered from greatest to least magnitude of difference. The statistical significance of the difference between the PBS and anti-VEGF eyes is assessed using a Wilcoxon signed-rank test. W=28; $p \leq 0.05$. The OCT B-scans in (b,c) show representative lesions from mice intravitreally injected with PBS and anti-VEGF respectively. Both images are from mouse 5.

The same lesions were then assessed for PT signal density. As reported in Figure 14, eyes given the anti-VEGF intervention showed a measurable reduction in photothermal signal density associated with laser lesions. Again, since each mouse had one eye treated with anti-VEGF and one eye treated with PBS, a paired analysis could be performed. In 6 of 7 eyes, the anti-VEGF treatment reduced lesion-associated photothermal signal density, as reported in Figure 14a. This

difference is statistically significant, and it indicates that physiological changes to the laser lesion microenvironment induced by anti-VEGF injections can be detected *in vivo* using PT-OCT and GNR technologies. Figure 14b-c shows representative laser lesions with photothermal signal overlaid. Both lesions are from the same mouse.

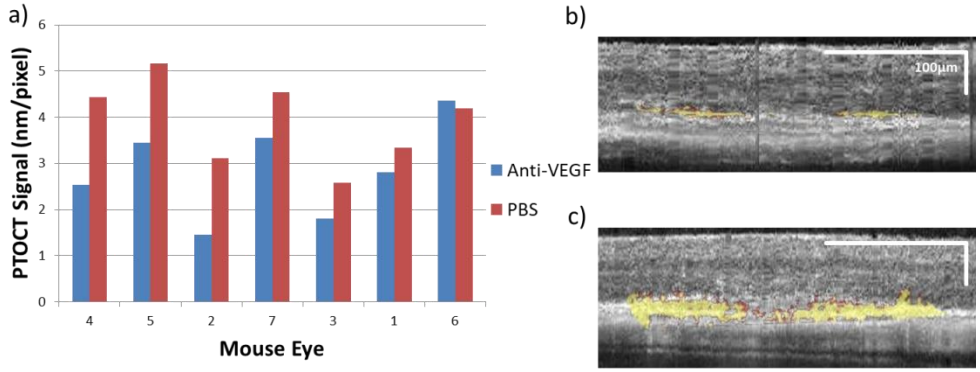

Figure 14: PTOCT of Targeted GNR With or Without Intravitreal Anti-VEGF *In Vivo*. (a) PT signal density from every eye in both experimental cohorts, paired by mouse (n=7 mice). The results are ordered from greatest to least magnitude of difference with the horizontal axis numbers matching the eyes to those in Figure 13(a). The statistical significance of the difference between the PBS and anti-VEGF eyes was assessed using a Wilcoxon signed-rank test. W=27; $p \leq 0.05$. (b,c) Representative images of OCT b-scans with overlaid lesion-associated photothermal signal, both from mouse 5. (b) shows a lesion from the eye given the anti-VEGF injection, while (c) is from the PBS-injected control eye of the same mouse, which shows both a larger lesion and increased PT signal per pixel.

Discussion

OCT is the clinical gold standard in retinal imaging because it provides quick, easy, and highly detailed structural information about its target. However, it is limited due to its inability to generate physiological information about the tissues it images, since this information can provide valuable information about disease states or responses to therapy. Our goal with this research was to improve OCT by adding to it the ability to detect endogenous and exogenous contrast agents *in vivo* in the retina, and thereby improve the ability of OCT to image physiological processes.

Regarding endogenous contrast agents, we show that RPE-associated melanin can be readily imaged in the mouse retina. We also demonstrate that there are no non-melanin sources of endogenous contrast in the retina. This is the first time retinal melanin has been directly imaged using OCT adjuncts, which is important because it could allow for rapid assessment of the health of the RPE layer in research and clinical settings. Some diseases have altered RPE and melanin distribution in the retina, notably AMD, and imaging of endogenous melanin using PT-OCT could provide useful information about this disease in the future.

Regarding exogenous contrast agents, we show that both targeted and untargeted GNR accumulation in laser lesions is detectable using PT-OCT. To demonstrate this, we used PT-OCT to image laser lesions in mice injected with PBS, untargeted GNR, or targeted GNR. We were able to detect the accumulation of both targeted and untargeted GNR in laser lesions using PT-OCT, but while there was a higher photothermal signal density in lesions from the targeted vs the untargeted group, this difference was not statistically significant. Part of the failure to achieve significance is likely due to the inherent variability of the LCNV model[58].

Additionally, these data suggest that a large proportion of the accumulation seen in the targeted GNR cohort is due to passive accumulation of GNR rather than active targeting due to surface antibodies. The exact mechanism by which fairly large GNR passively accumulate in LCNV lesions, or indeed in any tissue with abnormal vasculature, has yet to be elucidated. However, since we are using PT-OCT to detect the GNR, we know that they must be relatively immobile in the tissue being imaged to generate a photothermal signal that we can detect[59]. In the LCNV model specifically, it has been shown that rodent lesions are at their leakiest 4-7 day after lasering, and our imaging was performed in this window[58]. Additionally, it is understood that these lesions have abnormal hemodynamics leading to areas of very slow moving or even

static blood, which could increase GNR accumulation[60]. The vasculature itself is leaky, and although these GNR are on the edge in terms of size of what has been shown to extravasate in similar conditions, this is a possibility as well[61].

These effects are likely also related to our choice of an 8 hour post-injection imaging time point. Longer waiting periods could allow for increased clearance of unbound GNR from the lesions. A potentially useful theoretical model for the availability in tissue of immobilized GNR for PT-OCT imaging can be constructed by considering the rates of influx of GNR into tissue from the vascular circulation as well as clearance of GNR from tissue into the vasculature. The higher the GNR concentration in the damaged vasculature, the faster it should accumulate in tissue. Any force that prevents the egress of GNR from the tissue back into the vasculature will also increase the tissue concentration at a given time point. It is a reasonable hypothesis, then, that the targeting effect from antibodies on the GNR surface might be more apparent at time points past 24 hours, when the untargeted GNR have had time to be cleared from the tissue based on similar previous studies in tumor models[62], while antibody binding might hold the targeted GNR in place. As previously stated, this is a theoretical model that might have relevance for future experimental design rather than anything derived from our current data. Indeed, it is difficult to assess to what degree the GNR being detected are truly immobilized in extravascular spaces versus being relatively immobile in abnormal lesion-associated vasculature, which complicates any theoretical understanding of GNR clearance rates.

Finally, we assessed our ability to use exogenous contrast agents to detect physiological changes in the retina. Again using the LCNV model, we added intravitreal anti-VEGF treatment (or contralateral PBS controls) immediately following lasering to the experimental protocol, while also intravenously injecting targeted GNR on day 5 post-lasering. This allowed us to

perform a paired-eye analysis of the effects of anti-VEGF treatments on GNR accumulation. First, we report that as expected the treatment reduces LCNV lesion diameter to a statistically significant degree, which demonstrates the efficacy of the injections. Then, we assess the anti-VEGF vs PBS cohorts for changes in photothermal signal density using PT-OCT. We found that there were statistically significant changes to signal density between these cohorts, likely due to changes in the extent of neovascular growth in the lesions. This differential GNR accumulation also likely represents changes in the functional ability of the existing or new vasculature in the lesions to prevent the extravasation of GNR into the surrounding tissue. In the future, this type of detection of physiological change using OCT imaging adjuncts could lead to improvements in health outcomes related to vision loss.

There are a number of challenges associated with PT-OCT imaging of the retina *in vivo*, including the presence of endogenous contrast from melanin in the RPE layer. While, as discussed previously, this could have certain benefits to future applications of PT-OCT technology, it presents a difficulty in the detection of exogenous contrast agents like GNR. We use ROI selection to minimize this problem, but future improvements to both GNR size and targeting, to improve accumulation, and to PT-OCT technology, could offer solutions to this problem. We could tune the GNR and PT-OCT systems to operate in the NIR region, which should somewhat reduce the amount of photothermal signal generated by melanin. Additionally, we could alter our imaging time points and biomarker selection to optimize GNR accumulation. One interesting idea would be to evaluate photothermal signal at multiple wavelengths in tissue, which could improve our ability to distinguish exogenous from endogenous contrast. Despite these difficulties, in this study we were able to achieve our major goal of adding physiological information to OCT images.

Chapter 4: *In Vitro* Imaging of Intracellular GNR Using Spectral Fractionation Optical Coherence Tomography

Introduction

We demonstrated success in using PT-OCT to image GNR *in vivo* in the retina, but there were some limitations to the approach. So, we experimented with additional OCT adjuncts that might be useful for contrast enhancement of OCT. One such adjunct is spectral-fractionation OCT (SF-OCT)[30]. SF-OCT assesses the ratio between the amplitudes of shorter versus longer wavelengths returned as part of the native OCT signal from imaging targets. This technology allows for the detection of spectral changes in the backscatter from a tissue, endogenous or exogenous, that would be missed by a standard analysis of OCT data. There are considerable practical advantages to this approach. It detects strong spectrally and spatially localized scatterers that can be present at relatively low concentrations in tissue, where previous spectral OCT research relied on high concentrations of absorbing adjuvants, e.g. dyes[15,63,64].

Additionally, SF-OCT does not require additional light sources or detectors, but merely additional analysis of already existing OCT data which is an advantage over other OCT adjuncts discussed in chapter one, as well as representing an easier path to implementation than those that require, for example, dual-band OCT utilizing two distinct light sources[63]. In short, implementation of SF-OCT only requires a software upgrade, rather than a hardware one. The only notable drawback to SF-OCT is that spectral resolution (the ability to detect less strong shifts in backscattered spectra) comes at the expense of spatial resolution. However, as OCT systems generally have spatial resolution to spare, we consider this a suitable tradeoff[65].

With their strong reflection of light at specific, tunable wavelengths due to their SPR, GNR are ideal candidates to generate contrast using SF-OCT[66]. With our goal being translational

applications of GNR that provide contrast enhancement to OCT, we decided to assess our ability to move GNR intracellularly and image them in that environment, which we hadn't done previously. These studies are translationally relevant given the proliferation of cell-based therapies currently being advanced. First, we tested whether or not we could detect GNR in water or tissue phantoms using SF-OCT. Then, we tested our ability to use SF-OCT to image intracellularly localized GNR, also in tissue phantoms. The work discussed in this chapter is the result of a collaborative effort, and has been published in Jia et al. (Optics Express, 2015)[30]. Figures 16 and 17 are reprinted here with permission from the author.

Methods

OCT Imaging System and Image Analysis

All imaging was conducted using a commercial FD-OCT system (RTVue-XR, Optovue, Fremond, CA) centered at 840 nm. The system was modified to allow the use of the raw spectral data it generated. This spectral data was separated into short and long wavelength halves with the split at 840nm. The halves were further split into four separate groups used to generate independent A-scans which were subsequently averaged for short- and long-wavelength spectral intensities. A ratio of these intensities known as a SLoW (short-long wavelength) ratio was generated and evaluated for every pixel above an intensity threshold of 3SD over the mean intensity of a scan. For a complete explanation of how the SLoW ratio is derived from raw OCT data, please see Jia et al. (Optics Express, 2015)[30]. Since the GNR being imaged by this system have an SPR at a longer wavelength than the middle of the OCT system spectrum, the "long" wavelengths of the short:long wavelength ratio will be increased. This is reported here as a negative SLoW ratio, in units of dB.

GNR Constructs

The GNR used for the studies reported in this chapter had an SPR of 870nm after being diluted. Aside from this difference, GNR functionalization was performed as described in chapter 2 to generate bare GNR and Tat-GNR. Quality assurance measures were performed as discussed in that chapter.

GNR in Tissue Phantoms and RPE Cells

For experiments involving GNR suspended in tissue phantoms, the phantoms were created via the serial dilution of intralipid 20% solution (Intralipid 20% emulsion, Sigma-Aldrich, St. Louis, MO) down to 0.1%. GNR as previously described were diluted to concentrations of 5x10^10 GNR/mL using the already-diluted intralipid solution. The final phantom had a concentration of 5x10^10 GNR/mL in 0.1% intralipid. All imaging was done using 5mL tissue phantoms in 10mL test tubes.

To localize GNR intracellularly, wells containing agar coated with 5x10^5 aRPE-19 cells were incubated with 10^9 Tat-GNR for 4 hours at 37 degrees celcius, followed by rinsing to remove excess GNR. Following treatment with trypsin, cells were concentrated via centrifugation and fixed using a 1% solution of neutral buffered formalin (NBF). Figure 15 is a TEM image that shows were successful in loading GNR into cells, and that the GNR were concentrated in cytoplasmic vesicles inside the cells. Cells were resuspended in 1% gelatin for subsequent imaging.

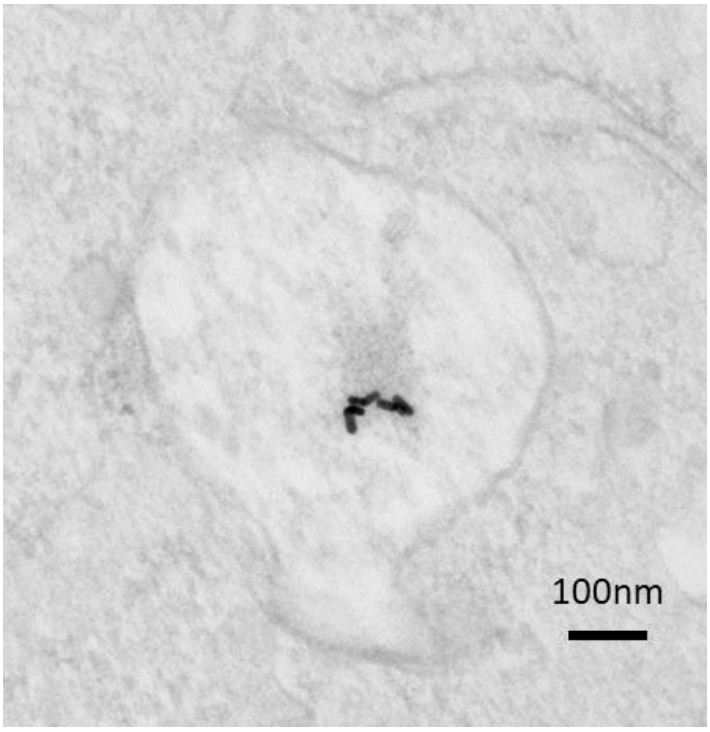

Figure 15: TEM of Intracellular Tat-GNR. This representative image demonstrates that the Tat-GNR move intracellularly following incubation with aRPE-19 cells, and in fact that they are in vesicles inside of those cells.

Results

SF-OCT Imaging of GNR in Tissue Phantom

Initial SF-OCT imaging of GNR took place using standard CTAB-coated "bare" GNR suspended in tissue phantoms. Using SLoW ratio cutoffs of +/- 1dB to separate intralipid from GNR, three types of phantom were imaged and the results are reported in Figure 16. Figure 16a shows the intralipid solution, which has no detectable spectral shift. Figure 16b demonstrates that bare GNR suspended in water generate a considerable spectral shift, in this case color-coded red, and figure 16c demonstrates that GNR in intralipid still produces a detectable spectral shift despite the noisier background. These findings demonstrate that bare GNR can be detected using SF-OCT in water and in tissue phantoms.

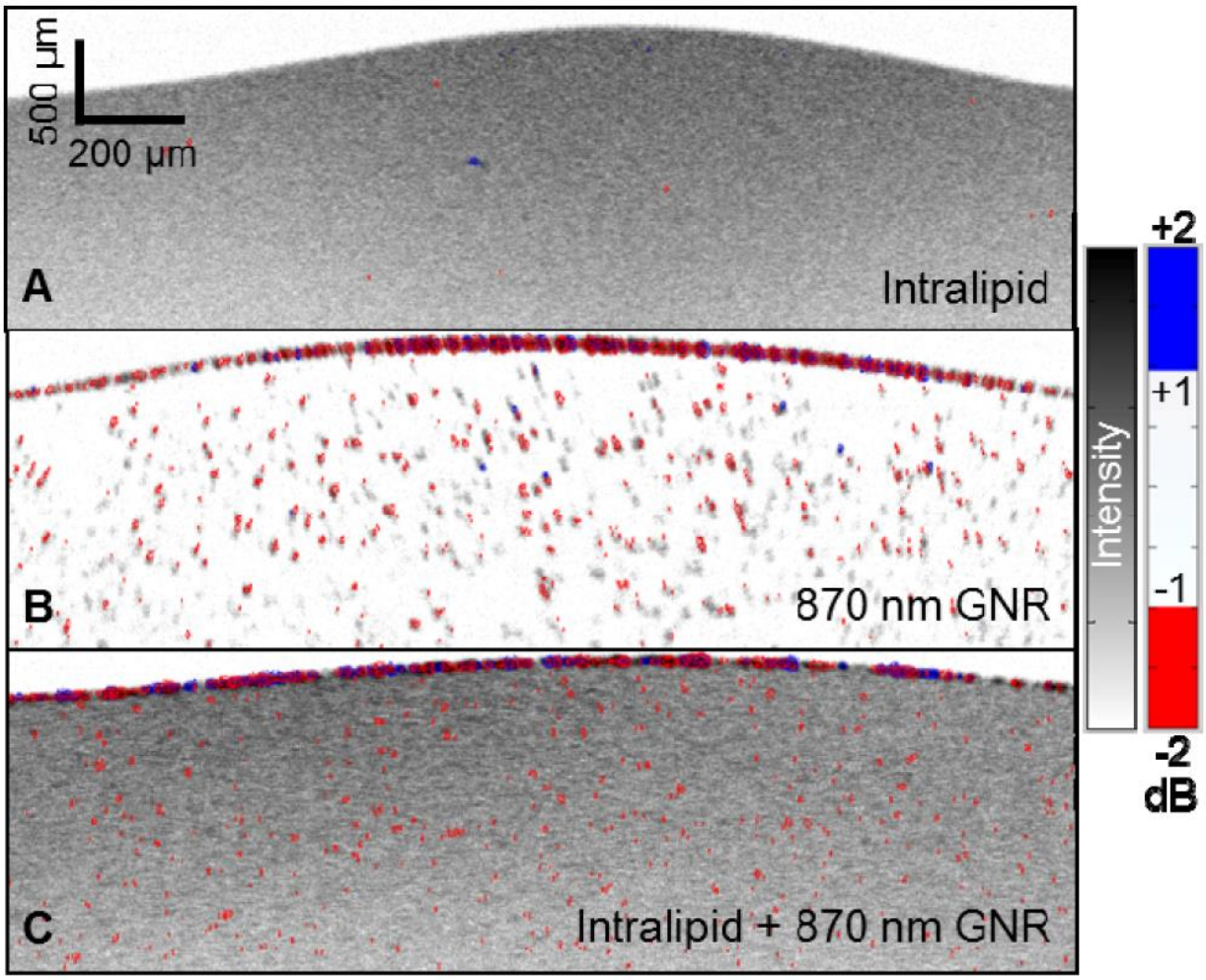

Figure 16: SF-OCT Imaging of GNR in Water and Tissue Phantom. SF-OCT imaging of (a) 0.1% intralipid, (b) GNR in water, and (c) GNR in intralipid. The OCT image is in grayscale, with SF-OCT SLoW ratios colored in blue or red for +1 and -1 dB ratio measurements, respectively. The GNR are plainly visible in red in water and intralipid due to their increasing the long portion of the SLoW ratio. Reprinted with permission of authors from Jia et al. (Optics Express, 2015)[30].

SF-OCT Imaging of GNR in RPE Cells

Consistent with our overarching goal of translational imaging of contrast agents using OCT, we next imaged RPE cells that had been incubated with Tat-GNR (labeled cells) in a tissue phantom. As controls, we used the phantom without any cells, as well as the phantom with cells that were not incubated with GNR (unlabeled cells).

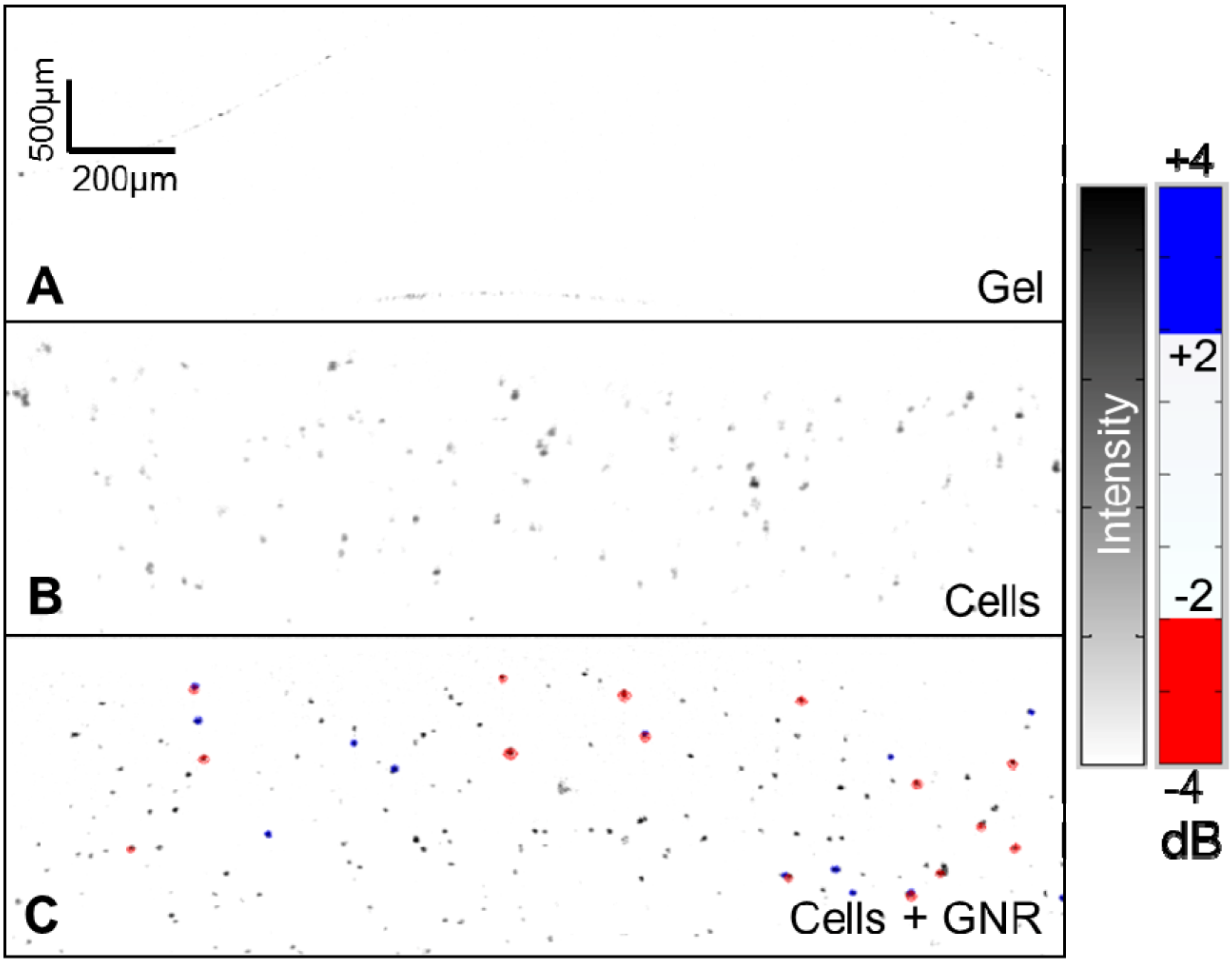

Figure 17: SF-OCT Imaging of Intracellular GNR in Tissue Phantoms. SF-OCT images of (a) 1% gelatin, (b) aRPE-19 cells fixed and suspended in 1% gelatin, and (c) aRPE-19 cells previously incubated with Tat-GNR fixed and suspended in 1% gelatin. The SLoW ratio cutoffs here are moved to +/- 2dB. The characteristic SLoW ratio associated with GNR used in this study is still detectable in (c) even when the GNR are intracellularly localized. Reprinted with permission of authors from Jia et al. (Optics Express, 2015)[30]

The SLoW ratio cutoffs used in this study were +/- 2 dB, based on the more variable signal from unlabeled RPE cells versus the background in the previous experiment. Figure 17 shows that there was some positive (short-wavelength dominant) signal from the unlabeled RPE cells in the phantom (Figure 17b), and there was the expected considerable negative SLoW signal associated with labeled RPE cells suspended in a tissue phantom (Figure 17c). Of note, some of the labeled RPE cells had a positive SLoW signal, which could be due to characteristics of RPE cells, or due to aggregation of the GNR intracellularly following cell uptake. Some side-

by-side aggregation would be consistent with these results and the findings shown in Figure 15. There was no detectible spectral signal from the phantom itself (Figure 17a).

Discussion

This brief chapter focuses on some of the exciting results obtained by SF-OCT imaging of GNR. The SPR of the GNR was chosen to be offset from the center of the OCT systems, in order to maximally impact the SLoW ratio. This is a different design principle than our initial studies which sought to align the center wavelength of the OCT system and the GNR SPR in order to generate maximal scattering and absorption from the GNR.

We demonstrate that GNR can be detected using SF-OCT in a tissue phantom, which is a valuable proof of principle. Additionally, this detection comes while maintaining a clinically useful resolution (15nm) for the OCT system. More importantly, we demonstrate that we are able to detect intracellularly localized GNR in labeled cells suspended in a phantom. Given the negative results from the unlabeled cells, this result shows both that our GNR construct succeeded in entering cells in concentrations sufficient for detection, and that we could use GNR with SF-OCT for the generation of intracellular contrast in tissue phantoms. This is the first time this has been demonstrated, and it shows promise for future implementations of GNR and SF-OCT technology.

Chapter 5: Summary and Conclusions

The goal of translational imaging research is to improve the breadth, accuracy, and timeliness of information available for assessment prior to making clinically important decisions. For this reason, significant improvements in healthcare often are the result of innovations in imaging technologies. The goal of our research has been to improve optical coherence tomography in ways that could potentially be clinically translatable. OCT is already a mainstay of clinical ophthalmology because of its speed, resolution, and general ease of use. However, its major drawback is that it can generally only give us structural information about the tissue it is being used to image.

The physical nature of OCT limits its native scope to structural information and also makes it difficult to design contrast agents that are compatible with it. Since OCT is fundamentally a form of interferometry, it cannot image fluorophores, for example, that might be used with other *in vivo* imaging modalities to provide contrast enhancement[13]. So, we needed a contrast agent with the potential to interact with OCT systems by absorbing or reflecting the light emitted and detected by the systems. Gold nanorods fit our contrast agent needs well, as they have versatile optical properties and gold is considered biocompatible.

Our initial experiments simply involved the construction and testing of various GNR constructs for OCT imaging. The injection of bare (more accurately, CTAB-coated) GNR into the vitreous caused the rapid formation of an amorphous opacity that degraded imaging capabilities, which was consistent with results that were published at the same time as we were performing these experiments. That publication also showed an immune response to the bare GNR injections in the mouse eye[36]. After realizing this reaction was taking place, we moved to "detoxify" our GNR by replacing the surface CTAB with PEG, which is also considered to be

biocompatible[38]. While we didn't assess for immune response to this GNR construct directly, we were at least able to inject them intravitreally and image them successfully, without it causing gross morphological abnormalities in the eye.

These intravitreal studies showed us that PEG-coated GNR were viable constructs for *in vivo* imaging experiments, but that they weren't able to pass into the retina from the vitreous. This is not unexpected based on their size. So we moved to intravenous injections of GNR to try to study them in the retina. In order to have a good target for our imaging, we used the LCNV model to provide localized lesions onto which we could focus our search[42]. Our attempts to image GNR natively on OCT were unsuccessful though, since the heterogeneous tissue of the retina and of LCNV lesions in particular created too much scattering noise to detect GNR on top of it.

This left us with a problem, since we thought we had a way to deliver GNR to the retina and could perform *in vivo* OCT imaging in a relevant animal model, but we couldn't see our contrast agent. This led to our establishing collaborations with labs that work on OCT adjuncts, which broadly defined are technologies that work in cooperation with OCT systems to provide additional data about the imaging targets.

The first of these we discuss is PT-OCT, and this work was done in collaboration with the Skala lab and resulted in two publications[16,56]. Our early experiments established that there is already an endogenous absorber in the mouse retina, melanin, which is present in the RPE layer. This result was both exciting and frustrating. It presents an imaging target that has potential clinical value in AMD or ocular melanoma, for example. Since this imaging requires no contrast injections and uses laser powers generally considered permissible in humans, it might be our

most immediately translatable experimental result. However, the clinical utility of improved melanin quantification in the retina has yet to be proven.

This very strong endogenous contrast agent represented a considerable source of background noise for subsequent studies imaging injected GNR in the LCNV model. Much of our experimental protocol was designed to minimize this background signal, from the choice of 5 days post-lasering for our studies to our decision to use blinded hand-selected ROI to assess for the presence of our contrast agent, which introduces human error and is quite time consuming. The photothermal signal from melanin is currently a barrier to clinical translation of GNR imaging using PT-OCT.

Despite this difficulty, we were able to achieve positive and novel results from our studies of PT-OCT imaging of intravenously delivered GNR. We found we could detect both untargeted and ICAM2-targeted GNR in LCNV lesions *in vivo* using PT-OCT. While we couldn't distinguish between these two GNR constructs, there was a trend toward a stronger signal from the targeted GNR, which is consistent with a targeting effect. Our most exciting result came with the final experiment discussed in Chapter 3. We detected anti-VEGF-induced changes in targeted GNR accumulation in LCNV lesions. The combination of LCNV, used to model wet AMD, and anti-VEGF injections, used to treat wet AMD, maintained the translational relevance of this study. Our ability to detect these clinically relevant physiological changes, likely a result of vascular changes caused by anti-VEGF, fulfilled the major goal of our imaging studies with OCT and GNR – we were able to move OCT beyond the realm of structural imaging.

An interesting question considered in detail in Chapter 3 is why there is so much apparent accumulation of untargeted gold nanorods in LCNV lesions in that study. While the answer is

uncertain, it likely involves altered hemodynamics in the lesion as well as damaged or destroyed vasculature permitting the extravasation of GNR into surrounding lesion tissue[60]. This is an important distinction however, as one might expect untargeted GNR in areas of static blood flow to eventually clear from the lesions, while targeted GNR held by antibody-antibody interactions might not. This would argue in favor of assessing longer post-injection time points for future imaging studies using targeted GNR. A relevant piece of evidence in Chapter 2 is the immunohistochemical study of flat mounted retinas treated in the LCNV model and injected with targeted vs untargeted nanorods. This protocol was essentially identical to that used in Chapter 3. While not quantitative, the results suggest a much higher concentration of targeted GNR relative to untargeted GNR in LCNV lesions. While there are issues with the quality of this image, these disparate results might suggest that the process of flat mounting itself might remove some of the unbound GNR from the lesions, which allows the apparent targeting effect of IHC to be consistent with the lack of one of PT-OCT imaging. This does highlight one of the issues with the studies we discuss. We were largely unable to perform further optimization of GNR constructs, molecular targets, or imaging protocols due to the time required to perform each set of experiments.

In addition to using PT-OCT as an adjunct to image GNR, we also conducted some experiments with the Huang lab using SF-OCT to detect GNR, although these experiments were conducted in tissue phantoms[30]. SF-OCT was able to detect GNR embedded in tissue phantoms. More importantly, it was also able to detect these GNR after they were taken up by RPE cells, and the cells themselves were embedded in a tissue phantom. This demonstrates that our GNR can interact with the light from OCT systems even from an intracellular position, an example of their versatility as contrast agents for use with OCT adjunct technologies.

PT-OCT and SF-OCT have their own strengths and weaknesses as OCT adjuncts. PT-OCT requires an additional laser source, which SF-OCT does not. Additionally, PT-OCT takes much longer to complete a scan of a given area than SF-OCT, and this can be as long as 40 minutes for scanning a complete LCNV lesion. On these counts, SF-OCT has considerably fewer barriers to clinical translation. However, in generating its spectral data SF-OCT compromises its spatial resolution to a degree, and this spatial resolution is one of the major advantages of OCT as a clinical tool. Also, at least in our studies, SF-OCT of GNR has not yet been demonstrated *in vivo* in the eye, while PT-OCT has. Finally, PT-OCT can image a potentially useful endogenous contrast source without the need for additional exogenous contrast agents, which improves the translatability of this technology. Considering these characteristics, both technologies appear to have a path toward clinical translation.

Regarding translation of the work into a clinical setting, some thought should be given to the patient populations that may benefit if retinal physiology and molecular expression are able to be visualized by OCT systems, with or without exogenous contrast agents. Regarding the leading causes of blindness, there are certain patient populations that are more likely to suffer vision loss from the worsening of their disease. The easiest way to identify these patients, and therefore select candidates for this novel imaging, would be simply to screen those people with pre-existing less severe disease, including diabetic patients (for DR-related changes), patients with drusen (for progression to wet AMD), or patients with elevated intraocular pressure (for incipient glaucoma). If contrast-enhanced OCT represents a greater time or risk burden for patients than standard OCT imaging, this type of pre-screening could maintain the translatability of the technology while still allowing it to identify the majority of patients who would benefit from earlier disease detection and clinical intervention.

Bibliography

1. Huang D, Swanson EA, Lin CP, et al. Optical coherence tomography. *Science*. 1991;254(5035):1178-1181. https://www.ncbi.nlm.nih.gov/pubmed/1957169.

2. Schmidt-Erfurth U, Klimscha S, Waldstein SM, Bogunović H. A view of the current and future role of optical coherence tomography in the management of age-related macular degeneration. *Eye*. 2017;31(1):26-44. doi:10.1038/eye.2016.227

3. Garcia JMB de B, Isaac DLC, Avila M. Diabetic retinopathy and OCT angiography: Clinical findings and future perspectives. *Int J Retin Vitr*. 2017;3(1):1-10. doi:10.1186/s40942-017-0062-2

4. Hood DC. Improving our understanding, and detection, of glaucomatous damage: An approach based upon optical coherence tomography (OCT). *Prog Retin Eye Res*. 2017;57:46-75. doi:10.1016/j.preteyeres.2016.12.002

5. Midena E, Pilotto E. Emerging Insights into Pathogenesis. In: *Developments in Ophthalmology*. Vol 60. ; 2017:16-27. doi:10.1159/000459687

6. Rosenfeld PJ. Optical coherence tomography and the development of antiangiogenic therapies in neovascular age-related macular degeneration. *Investig Ophthalmol Vis Sci*. 2016;57(9):OCT14-OCT26. doi:10.1167/iovs.16-19969

7. Troutman TS, Barton JK, Romanowski M. Optical coherence tomography with plasmon resonant nanorods of gold. *Opt Lett*. 2007;32(11):1438. doi:10.1364/ol.32.001438

8. Hu M, Chen J, Li ZY, et al. Gold nanostructures: Engineering their plasmonic properties for biomedical applications. *Chem Soc Rev*. 2006;35(11):1084-1094. doi:10.1039/b517615h

9. Zysk AM, Nguyen FT, Oldenburg AL, Marks DL, Boppart SA. Optical coherence tomography: a review of clinical development from bench to bedside. *J Biomed Opt*. 2007;12(5):051403. doi:10.1117/1.2793736

10. Fisher RF. New Directions in Ophthalmic Research. *Br J Ophthalmol*. 2007;67(4):271-271. doi:10.1136/bjo.67.4.271

11. Alex A, Považay B, Hofer B, et al. Multispectral in vivo three-dimensional optical coherence tomography of human skin. *J Biomed Opt*. 2010;15(2):026025. doi:10.1117/1.3400665

12. Drexler W, Fujimoto JG. State-of-the-art retinal optical coherence tomography. *Prog Retin Eye Res*. 2008;27(1):45-88. doi:10.1016/j.preteyeres.2007.07.005

13. Boppart SA, Oldenburg AL, Xu C, Marks DL. Optical probes and techniques for molecular contrast enhancement in coherence imaging. *J Biomed Opt*. 2005;10(4):041208.

doi:10.1117/1.2008974

14. Oldenburg AL, Gunther JR, Toublan FJ, Marks DL, Suslick KS, Boppart SA. Magnetic contrast agents for optical coherence tomography. *Coherence Domain Opt Methods Opt Coherence Tomogr Biomed VIII*. 2004;5316(217):91. doi:10.1117/12.529119

15. Yaqoob Z, McDowell E, Wu J, Heng X, Fingler J, Yang C. Molecular contrast optical coherence tomography: a pump-probe scheme using indocyanine green as a contrast agent. *J Biomed Opt*. 2006;11(5):054017. doi:10.1117/1.2360525

16. Lapierre-Landry M, Gordon AY, Penn JS, Skala MC. In vivo photothermal optical coherence tomography of endogenous and exogenous contrast agents in the eye. *Sci Rep*. 2017;7(1):1-9. doi:10.1038/s41598-017-10050-5

17. Park K, Hsiao MS, Yi YJ, et al. Highly Concentrated Seed-Mediated Synthesis of Monodispersed Gold Nanorods. *ACS Appl Mater Interfaces*. 2017;9(31):26363-26371. doi:10.1021/acsami.7b08003

18. Attia YA, Vázquez-Vázquez C, Blanco MC, Buceta D, López-Quintela MA. Gold nanorod synthesis catalysed by Au clusters. *Faraday Discuss*. 2016;191:205-213. doi:10.1039/c6fd00015k

19. Xing L, Li D, Chen B, Dai Y, Wu W, Wang G. Enhancement of light absorption by blood to Nd:YAG laser using PEG-modified gold nanorods. *Lasers Surg Med*. 2016;48(8):790-803. doi:10.1002/lsm.22557

20. Leonov AP, Zheng J, Clogston JD, Stern ST, Patri AK, Wei A. Detoxification of Gold Nanorods by Treatment with Polystyrenesulfonate 聚苯乙烯磺酸pss修饰.pdf. 2008;2(12):2481-2488.

21. Ling T, Qingshan W, Alexander W, Ji-Xin C. Gold Nanorods as Contrast Agents for Biological Imaging: Optical Properties, Surface Conjugation and Photothermal Effects†. *Photochem Photobiol*. 2009;85(1):21-32. doi:10.1111/j.1751-1097.2008.00507.x

22. Takahashi H, Niidome Y, Niidome T, Kaneko K, Kawasaki H, Yamada S. Modification of gold nanorods using phosphatidylcholine to reduce cytotoxicity. *Langmuir*. 2006;22(1):2-5. doi:10.1021/la0520029

23. Hardin WG, Sokolov K V., Joshi PP, Yoon SJ, Emelianov S. Conjugation of Antibodies to Gold Nanorods through Fc Portion: Synthesis and Molecular Specific Imaging. *Bioconjug Chem*. 2013;24(6):878-888. doi:10.1021/bc3004815

24. Santhosh PB, Thomas N, Sudhakar S, Chadha A, Mani E. Phospholipid stabilized gold nanorods: Towards improved colloidal stability and biocompatibility. *Phys Chem Chem Phys*. 2017;19(28):18494-18504. doi:10.1039/c7cp03403b

25. Mahmoud NN, Al-Qaoud KM, Al-Bakri AG, Alkilany AM, Khalil EA. Colloidal stability of gold nanorod solution upon exposure to excised human skin: Effect of surface chemistry and protein adsorption. *Int J Biochem Cell Biol*. 2016;75:223-231. doi:10.1016/j.biocel.2016.02.020

26. Gomez L, Cebrian V, Martin-Saavedra F, Arruebo M, Vilaboa N, Santamaria J. Stability and biocompatibility of photothermal gold nanorods after lyophilization and sterilization. *Mater Res Bull*. 2013;48(10):4051-4057. doi:10.1016/j.materresbull.2013.06.034

27. Ashwath Jayagopal AYG. Engineering of Nanoscale Contrast Agents for Optical Coherence Tomography. *J Nanomed Nanotechnol*. 2014;s5(01). doi:10.4172/2157-7439.s5-004

28. Adler DC, Huang S-W, Huber R, Fujimoto JG. Photothermal detection of gold nanoparticles using phase-sensitive optical coherence tomography. *Opt Express*. 2008;16(7):4376. doi:10.1364/oe.16.004376

29. M.C. S, M.J. C, A. W, J.A. I. Photothermal optical coherence tomography of epidermal growth factor receptor in live cells using immunotargeted gold nanospheres. *Nano Lett*. 2008;8(10):3461-3467. doi:10.1021/nl802351p

30. Jia Y, Liu G, Gordon AY, et al. Spectral fractionation detection of gold nanorod contrast agents using optical coherence tomography. *Opt Express*. 2015;23(4):4212. doi:10.1364/oe.23.004212

31. Zhang EZ, Povazay B, Laufer J, et al. Multimodal photoacoustic and optical coherence tomography scanner using an all optical detection scheme for 3D morphological skin imaging. *Biomed Opt Express*. 2011;2(8):2202. doi:10.1364/BOE.2.002202

32. Nguyen VP, Li Y, Qian W, et al. Contrast Agent Enhanced Multimodal Photoacoustic Microscopy and Optical Coherence Tomography for Imaging of Rabbit Choroidal and Retinal Vessels in vivo. *Sci Rep*. 2019;9(1):5945. doi:10.1038/s41598-019-42324-5

33. Schol D, Fleron M, Greisch JF, et al. Anti-PSMA antibody-coupled gold nanorods detection by optical and electron microscopies. *Micron*. 2013;50:68-74. doi:10.1016/j.micron.2013.05.003

34. John R, Rezaeipoor R, Adie SG, et al. In vivo magnetomotive optical molecular imaging using targeted magnetic nanoprobes. *Proc Natl Acad Sci*. 2010;107(18):8085-8090. doi:10.1073/pnas.0913679107

35. Ni W, Kou X, Yang Z, Wang J. Tailoring longitudinal surface plasmon wavelengths, scattering and absorption cross sections of gold nanorods. *ACS Nano*. 2008;2(4):677-686. doi:10.1021/nn7003603

36. Gabriele Sandrian M, Wollstein G, Schuman JS, et al. Inflammatory response to intravitreal injection of gold nanorods. *Br J Ophthalmol*. 2012;96(12):1522-1529. doi:10.1136/bjophthalmol-2012-301904

37. Niidome Y, Nakamura Y, Honda K, et al. Characterization of silver ions adsorbed on gold nanorods: Surface analysis by using surface-assisted laser desorption/ionization time-of-flight mass spectrometry. *Chem Commun*. 2009;(13):1754-1756. doi:10.1039/b821402f

38. Calzoni E, Cesaretti A, Polchi A, Di Michele A, Tancini B, Emiliani C. Biocompatible Polymer Nanoparticles for Drug Delivery Applications in Cancer and Neurodegenerative

Disorder Therapies. *J Funct Biomater*. 2019;10(1):4. doi:10.3390/jfb10010004

39. Jordán J, Ruíz-Moreno JM. Advances in the understanding of retinal drug disposition and the role of blood–ocular barrier transporters. *Expert Opin Drug Metab Toxicol*. 2013;9(9):1181-1192. doi:10.1517/17425255.2013.796928

40. Kim JH, Kim JH, Kim KW, Kim MH, Yu YS. Intravenously administered gold nanoparticles pass through the blood-retinal barrier depending on the particle size, and induce no retinal toxicity. *Nanotechnology*. 2009;20(50):505101. doi:10.1088/0957-4484/20/50/505101

41. Ryan BYSJ. the Development of an Experimental Model of Disciform Macular Degeneration *. *Exposure*. 1979;LXXVII.

42. Dobi ET, Puliafito CA, Destro M. A New Model of Experimental Choroidal Neovascularization in the Rat. *Arch Ophthalmol*. 1989;107(2):264-269. doi:10.1001/archopht.1989.01070010270035

43. Montezuma SR, Vavvas D, Miller JW. Review of the ocular angiogenesis animal models. *Semin Ophthalmol*. 2009;24(2):52-61. doi:10.1080/08820530902800017

44. Grossniklaus HE, Kang SJ, Berglin L. Animal models of choroidal and retinal neovascularization. *Prog Retin Eye Res*. 2010;29(6):500-519. doi:10.1016/j.preteyeres.2010.05.003

45. Liu CH, Wang Z, Sun Y, Chen J. Animal models of ocular angiogenesis: From development to pathologies. *FASEB J*. 2017;31(11):4665-4681. doi:10.1096/fj.201700336R

46. Tobe T, Ortega S, Luna JD, et al. Targeted disruption of the FGF2 gene does not prevent choroidal neovascularization in a murine model. *Am J Pathol*. 1998;153(5):1641-1646. doi:10.1016/S0002-9440(10)65753-7

47. Giani A, Thanos A, Roh MI, et al. In vivo evaluation of laser-induced choroidal neovascularization using spectral-domain optical coherence tomography. *Investig Ophthalmol Vis Sci*. 2011;52(6):3880-3887. doi:10.1167/iovs.10-6266

48. Li T, Aredo B, Zhang K, et al. Phosphatidylserine (PS) is exposed in choroidal neovascular endothelium: PS-targeting antibodies inhibit choroidal angiogenesis in vivo and ex vivo. *Investig Ophthalmol Vis Sci*. 2015;56(12):7137-7145. doi:10.1167/iovs.15-17302

49. Shen WY, Yu MJT, Barry CJ, Constable IJ, Rakoczy PE. Expression of cell adhesion molecules and vascular endothelial growth factor in experimental choroidal neovascularisation in the rat. *Br J Ophthalmol*. 1998;82(9):1063-1071. doi:10.1136/bjo.82.9.1063

50. Staunton DE, Dustin ML, Springer TA. homologous to ICAM-1. 1989;339(May):61-64.

51. Lapierre-Landry M, Tucker-Schwartz JM, Skala MC. Depth-resolved analytical model

and correction algorithm for photothermal optical coherence tomography. *Biomed Opt Express*. 2016;7(7):2607. doi:10.1364/boe.7.002607

52. Kwak N, Okamoto N, Wood JM, Campochiaro PA. VEGF Is Major Stimulator in Model of Choroidal AND. *Invest Ophthalmol*. 2000;41(10):3158-3164.

53. Lin M, Hu Y, Chen Y, et al. Impacts of hypoxia-inducible factor-1 knockout in the retinal pigment epithelium on choroidal neovascularization. *Investig Ophthalmol Vis Sci*. 2012;53(10):6197-6206. doi:10.1167/iovs.11-8936

54. Campa C, Kasman I, Ye W, Lee WP, Fuh G, Ferrara N. Effects of an Anti-VEGF-A monoclonal antibody on laser-induced choroidal neovascularization in mice: Optimizing methods to quantify vascular changes. *Investig Ophthalmol Vis Sci*. 2008;49(3):1178-1183. doi:10.1167/iovs.07-1194

55. Sulaiman RS, Merrigan S, Quigley J, et al. A novel small molecule ameliorates ocular neovascularisation and synergises with anti-VEGF therapy. *Sci Rep*. 2016;6(April):1-11. doi:10.1038/srep25509

56. Gordon AY, Lapierre-Landry M, Skala MC, Penn JS. Photothermal Optical Coherence Tomography of Anti-Angiogenic Treatment in the Mouse Retina Using Gold Nanorods as Contrast Agents. *Transl Vis Sci Technol*.

57. Guizar-Sicairos M, Thurman ST, Fienup JR. Efficient subpixel image registration algorithms. *Opt Lett*. 2008;33(2):156-158. http://www.ncbi.nlm.nih.gov/pubmed/18197224.

58. Hoerster R, Muether PS, Vierkotten S, Schröder S, Kirchhof B, Fauser S. In-vivo and ex-vivo characterization of laser-induced choroidal neovascularization variability in mice. *Graefe's Arch Clin Exp Ophthalmol*. 2012;250(11):1579-1586. doi:10.1007/s00417-012-1990-z

59. Chhetri RK, Blackmon RL, Wu W-C, et al. Probing biological nanotopology via diffusion of weakly constrained plasmonic nanorods with optical coherence tomography. *Proc Natl Acad Sci*. 2014;111(41):E4289-E4297. doi:10.1073/pnas.1409321111

60. Asrani S, Zou S, D'Anna S, Phelan A, Goldberg M, Zeimer R. Selective visualization of choroidal neovascular membranes. *Investig Ophthalmol Vis Sci*. 1996;37(8):1642-1650.

61. Tolentino MJ, Husain D, Theodosiadis P, et al. Angiography of fluoresceinated anti-vascular endothelial growth factor antibody and dextrans in experimental choroidal neovascularization. *Arch Ophthalmol*. 2000;118(1):78-84. doi:10.1001/archopht.118.1.78

62. Tucker-Schwartz JM, Beavers KR, Sit WW, Shah AT, Duvall CL, Skala MC. In vivo imaging of nanoparticle delivery and tumor microvasculature with multimodal optical coherence tomography. *Biomed Opt Express*. 2014;5(6):1731. doi:10.1364/boe.5.001731

63. Kim TS, Jang S-J, Oh N, et al. Dual-wavelength band spectroscopic optical frequency domain imaging using plasmon-resonant scattering in metallic nanoparticles. *Opt Lett*. 2014;39(10):3082. doi:10.1364/ol.39.003082

64. Yang C, Choma MA, Simon J, Izatt J. Spectral triangulation molecular contrast OCT with indocyanine green as the contrast agent. 2014;29(17):SB3. doi:10.1364/bio.2004.sb3

65. Ghanta RK, Morgner U, Schuman JS, Drexler W, Fujimoto JG, Kärtner FX. Ultrahigh-resolution ophthalmic optical coherence tomography. *Nat Med*. 2002;7(4):502-507. doi:10.1038/86589

66. Oldenburg AL, Hansen MN, Zweifel DA, Wei A, Boppart SA. Plasmon-resonant gold nanorods as low backscattering albedo contrast agents for optical coherence tomography. *Opt Express*. 2006;14(15):6724. doi:10.1364/oe.14.006724